Journal of Colloid and Interface Science 687 (2025) 461–470

Contents lists available at ScienceDirect

Journal of Colloid And Interface Science

journal homepage: www.elsevier.com/locate/jcis

Regular Article

Crystal facet-induced reconstruction of MoN-supported Co pre-catalysts for optimized active sites and enhanced alkaline hydrogen evolution

Chaoran Pi [a,f,g,1], Difei Leng [b,1], Xuming Zhang [c,d,*], Shuangjie Wu [e], Yun Li [e], Li Huang [e], Zhihong Liu [a], Paul K. Chu [d,**], Kaifu Huo [f,g,**]

[a] Key Laboratory of Flexible Optoelectronic Materials and Technology, Ministry of Education, School of Optoelectronic Materials & Technology, Jianghan University, Wuhan 430056, China
[b] State Key Laboratory of Silicate Materials for Architectures, Wuhan University of Technology, Wuhan 430070, China
[c] The State Key Laboratory of Refractories and Metallurgy, Institute of Advanced Materials and Nanotechnology, Wuhan University of Science and Technology, Wuhan 430081, China
[d] Department of Physics, Department of Materials Science and Engineering, and Department of Biomedical Engineering, City University of Hong Kong, Tat Chee Avenue, Kowloon, Hong Kong, China
[e] Guizhou Wujiang Hydropower Development Co., Ltd., Guizhou 550002, China
[f] Wuhan National Laboratory for Optoelectronics (WNLO), School of Optical and Electronic Information, Huazhong University of Science and Technology, Wuhan 430074, China
[g] Research Institute of Huazhong University of Science and Technology in Shenzhen, Shenzhen 518057, China

HIGHLIGHTS

- Proposing a crystal facet-induced strategy for regulating reconstructed species.
- Inducing the transformation from Co metal to $Co(OH)_2$ (001) by MoN (002) matrix.
- Revealing the dissolve and re-deposit mechanism of Co under reducing environment.
- Achieving a 58 % reduction in overpotential over the reconstruction process.
- The reconstructed-catalyst retains 99.4 % of its activity after 110 h of test.

GRAPHICAL ABSTRACT

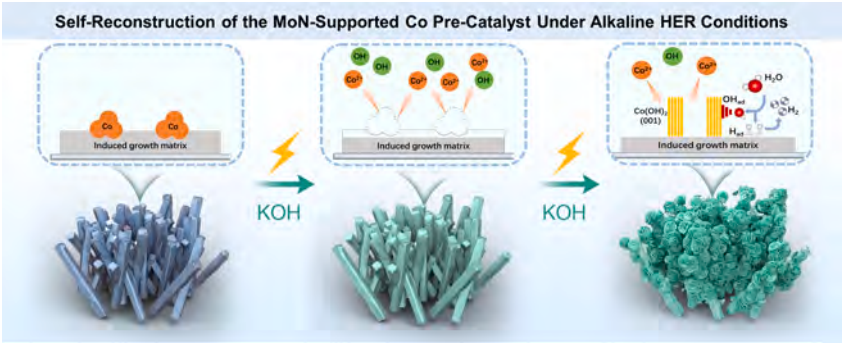

ARTICLE INFO

Keywords:
Crystal facet-induced reconstruction
Pre-catalyst
Optimized active sites

ABSTRACT

The self-reconstruction of electrocatalysts during the cathodic hydrogen evolution reaction (HER) has garnered significant interest due to its impact on microstructure and electrocatalytic efficiency. Understanding the mechanisms driving this transformation is crucial for the development of high-performance HER pre-catalysts. In this study, an efficient $Co(OH)_2$ (001)/MoN (002) heterostructured catalyst is fabricated through the self-reconstruction of the Co/MoN pre-catalyst and the mechanism of facet-induced reconstruction is investigated

* Corresponding author at: The State Key Laboratory of Refractories and Metallurgy, Institute of Advanced Materials and Nanotechnology, Wuhan University of Science and Technology, Wuhan 430081, China.
** Corresponding authors.
E-mail addresses: xumzhang@wust.edu.cn (X. Zhang), paul.chu@cityu.edu.hk (P.K. Chu), kfhuo@hust.edu.cn (K. Huo).
[1] These authors contributed equally to this work.

https://doi.org/10.1016/j.jcis.2025.02.066
Received 30 December 2024; Received in revised form 10 February 2025; Accepted 11 February 2025
Available online 15 February 2025

Operando characterization
Alkaline hydrogen evolution reaction

in detail. This Co/MoN pre-catalyst exhibits an impressive 58 % reduction in overpotential at a constant current density of 100 mA cm^{-2} over 5 h. It ultimately achieves a low overpotential of 339 mV at 1 A cm^{-2}, outperforming commercial Pt/C under similar current conditions, while maintaining high current activity with 99.4 % retention after 110 h of continuous electrolysis. *Operando* characterizations and theoretical simulations reveal that metallic Co dissolves rapidly under bias as H^+ ions infiltrate the interstitial spaces, and the dissolved Co^{2+} ions preferentially deposit as $Co(OH)_2$ nanosheets. This deposition aligns with the (001) facet of $Co(OH)_2$ and the prominent (002) plane of the MoN matrix through lattice matching, exhibiting a very low interfacial formation energy. Density-functional theory analysis reveals that the alignment of the crystal facets between $Co(OH)_2$ (001) and MoN (002) enhances electron transfer and modulates the interface to boost the water dissociation and hydrogen adsorption activity and kinetics. Our results underscore the importance of precise control over the reconstruction process for cathodic HER and facilitate the development of advanced transition metal-based electrocatalysts for industrial alkaline hydrogen production.

1. Introduction

Alkaline water electrolysis (AWE) is a promising hydrogen production technique since it offers flexibility in converting renewable energies (solar, wind) into high-value chemicals [1]. However, the hydrogen evolution reaction (HER) in alkaline electrolytes exhibits sluggish kinetics compared to acidic electrolytes, primarily due to the multi-step processes involving H_2O adsorption and H-OH cleavage [2]. High-performance electrocatalysts are thus essential in order to accelerate the process, reduce the overpotentials, and achieve efficient hydrogen production. To eliminate the need for noble metals, which possess high intrinsic HER activity but are exorbitantly priced [3], developing transition metal (TM) electrocatalysts with rapid H-OH dissociation kinetics and moderate hydrogen adsorption energies (ΔG_{H^*}) holds paramount significance for efficient alkaline hydrogen electrosynthesis [4,5].

Several TM-based cathodic electrocatalysts with the optimized electronic structure and coordination environment have been synthesized based on their initial structure–activity relationship [6]. However, the interactions among the electrocatalysts and reactants, intermediates, products, or electrolytes during alkaline hydrogen evolution have been verified to cause partial or complete reconstruction of the pre-designed catalysts [7], leading to deviation of electrocatalytic performance from expectation [8,9]. Shi et al. have reported the *in situ* formation of $Co(OH)_2$ on the surface of Co_9S_8 nanosheets with abundant sulfur vacancies (Sv-Co_9S_8) under alkaline HER conditions for enhanced water dissociation [10]. Peng et al. have demonstrated rapid reconfiguration from CoC_2O_4 to $Co(OH)_2$, and when coupled with MXene, charge transfer is facilitated due to the reduction of the energy barrier of the Volmer step, leading to faster HER kinetics [11]. Although those reports emphasize the beneficial effects of reconstruction [12,13], the strategy is primarily used as an activation method for pre-catalysts [14,15], while there are limitations in controlling the crystal structure of the reconstructed species [16,17]. These limitations may result in the formation of inactive crystal facets, collapse of the pre-designed geometric structure [18], and reduced availability of active sites [19], consequently complicating the fundamental understanding of the underlying catalytic mechanism and hindering further improvement [20]. There have been a few reports to explore this intriguing area and it has been proposed that introducing a specific matrix to influence the reconstruction of active species can positively impact the electrocatalytic efficiency of alkaline hydrogen evolution [21]. However, the details of structural evolution must still be explored, and the enhancement mechanisms are still ambiguous.

In this study, a crystal facet-induced reconstruction strategy is employed to regulate the reconstructed active species and investigate the role of reconstructed $Co(OH)_2$ nanosheets in energy applications. The molybdenum nitride-supported metallic cobalt (Co–MoN) nanoarray is synthesized as the pre-catalyst based on prescreening with molecular docking and rational design. Combined spectroscopic and microscopic evidence corroborates that the MoN substrate facilitates the structural conversion from metallic Co to $Co(OH)_2$ (001) by matching the formation energy of the crystal facets under alkaline HER conditions. This results in the establishment of a $Co(OH)_2$ (001)/MoN (002) heterointerface, which concurrently minimizes the H-OH cleavage energy in water dissociation and optimizes the ΔG_{H^*} for fast H* adsorption/desorption and enhanced alkaline HER performance. This pre-catalyst achieves a 58 % reduction in the overpotential at a current density of 100 mA cm^{-2} within 5 h, eventually reaching a low overpotential of 339 mV at 1 A cm^{-2}. Notably, it maintains high current activity with 99.4 % retention after 110 h of continuous electrolysis. Our findings confirm that incorporating a specific matrix as the preferential template can promote the growth of the desired crystal faces in the reconstructed active species to controllably enhance the electrocatalytic activity. This revelation provides new insights and foundational guidance for understanding the structure-performance relationship and fosters the advancement of efficient alkaline HER pre-catalysts.

2. Experimental section

2.1. Chemicals

Cobalt (II) nitrate hexahydrate ($Co(NO_3)_2{\cdot}6H_2O$), Sodium molybdate dihydrate ($Na_2MoO_4{\cdot}2H_2O$), Ammonium molybdate ($(NH_4)_6Mo_7O_{24}{\cdot}4H_2O$), Urea ($(NH_2)_2CO$), Nafion117 solution (5 % concentration) and Platinum carbon powder (Pt/C, 20 wt%) were procured from Shanghai Aladdin Biochemical Technology Co., Ltd. Hydrochloric acid (HCl, 37 %), Sulfuric acid (H_2SO_4, 98 %), Nitric acid (HNO_3, 65 %), Acetone (CH_3COCH_3, 95 %) Ammonium fluoride (NH_4F, 96 %) and Potassium hydroxide (KOH) were obtained from Sinopharm Chemical Reagent Co., Ltd. (Shanghai, China). Carbon cloth (CC) was sourced from CeTech Co., Ltd. All chemicals were of analytical grade, and used without further purification.

2.2. Synthesis of the Co–MoN pre-catalyst

The Co–MoN nanoarrays were synthesized by a modified two-step method [22]. The cobalt molybdate ($CoMoO_4$) nanoarrays were prepared on a piece of CC. The commercial CC was cut into rectangular pieces with dimensions of 1 × 2 cm^2, activated in 0.5 M H_2SO_4, and washed with 3 M HCl, acetone, and DIW successively. 1.23 mmol $Na_2MoO_4{\cdot}2H_2O$ and 1.25 mmol $Co(NO_3)_2{\cdot}6H_2O$ were dissolved in 30 mL of DIW in a 50 mL Teflon autoclave. A piece of the freshly treated CC was also placed in the autoclave which was then heated to 90 °C for 2 h. After natural cooling, the sample was taken out, washed with water, dried naturally, and annealed in a tubular furnace at 600 °C for 1 h under ammonia atmosphere (NH_3) to produce the Co–MoN pre-catalyst.

2.3. Synthesis of single-phase MoN

Single-phase MoN electrode is prepared in two steps. 4 mmol $(NH_4)_2MoO_4$ and cleaned CC are added to 10 mL of DIW and heated in a water bath to 70 °C. 40 mL HNO_3 are added dropwise and stirred in a water bath for 60 min to obtain molybdenum oxide (MoO_3) covered CC. MoN on CC is prepared by a nitridation process similar to the

preparation of Co–MoN electrode.

2.4. Synthesis of Co metal

0.01 mol urea, 0.12 mol NH_4F, 2.5 mmol $Co(NO_3)_2{\cdot}6H_2O$, and 30 mL DIW are added to a 50 mL Teflon autoclave together with a piece of freshly treated CC. The autoclave is sealed and heated to 180 °C for 2 h. After natural cooling, the sample is taken out, rinsed with water, dried naturally, and annealed in a tubular furnace at 600 °C for 1 h under a mixture of Hydrogen/Argon (H_2/Ar = 1/9) to form Co metal electrode.

2.5. Materials characterization

Powder X-ray diffraction (XRD) was performed to determine the structure of the samples on the Rigaku/Smart Lab with a Cu K_α source (λ = 1.54056 Å), and Raman scattering was conducted using a 532 nm laser as the excitation source on the Horiba LabRAM HR Evolution Raman Microscope. Field-emission scanning electron microscopy (FE-SEM) was used to examine the morphology using the ThermoFisher/Apreo S HiVac. The field-emission transmission electron microscopy (FE-TEM) images and high-angle annular dark field (HAADF) images were obtained on the JEOL JEM-F200. The chemical states were determined by X-ray photoelectron spectroscopy (XPS, AXIS SUPRA+) with the peaks calibrated to the 284.8 eV C 1 *s* peak. Inductively-coupled plasma mass spectroscopy (ICP-MS) was carried out on the Agilent 7700x. BET surface area test was performed at −196 °C on a Micromeritics ASAP 2420 instrument.

2.6. In situ Raman scattering

In situ Raman scattering was performed on the Horiba LabRAM HR Evolution Raman Microscope equipped with the 532 nm laser. The electrochemical cell made of Teflon had a quartz window to protect the objective lens. A graphite rod and solid-state Ag/AgCl served as the counter and reference electrodes, respectively, while the as-prepared self-supporting sample with dimensions of 1 × 1 cm^2 was the working electrode. The plane of the sample was perpendicular to the incident laser. Raman spectra were recorded with a 60-second exposure time, and measurements were accumulated in duplicated during this period. The applied potentials were set at 0 V and −0.05 V using an electrochemical workstation (CHI 760E, Chenhua, China) as the light path was interfered with by the evolved hydrogen gas bubbles. All the potentials were referenced to the reversible hydrogen electrode (RHE).

2.7. Electrochemical evaluation

To prevent the impact of oxygen generated at the anode on the cathode catalyst, a divided H-type electrolyzer with a hydrophilic-oleophobic membrane was constructed. The cell was purged with nitrogen for 30 min prior to the test. The electrochemical measurements were carried out on a workstation (Bio-logical VMP 300) using a three-electrode configuration at room temperature in 1 M KOH. Hg/HgO with 1 M KOH as the inner reference electrolyte was the reference electrode, graphite was the counter electrode, and the as-prepared self-supporting sample was the working electrode. Each piece of the WE were sealed with epoxy in advance to expose an area of 1 cm^2. The potentials were referenced to the reversible hydrogen electrode (RHE) unless stated otherwise. Linear scan voltammetry (LSV) was performed at a scanning rate of 0.2 mV s^{-1} from −0.9 V to −1.6 V *versus*. HgO and the results were *iR* compensated with a compensation of 90 %. The final potentials were referenced to the reversible hydrogen electrode (RHE) according to the Nernst equation: E (RHE) = E (Hg/HgO) + 0.059 pH + 0.098 V. The Tafel plots show the dependence of the steady-state current densities on overpotentials. Generally, the overpotential (η) is logarithmically related to the current density (j), and the linear portion of the Tafel plot is fitted to the Tafel equation: $\eta = a + b \log |j|$, where b is the Tafel slope. Cyclic voltammetry (CV) was carried out at different scanning rates (20, 40, 60, 80, and 100 mV s^{-1}) in the non-Faradaic potential range to derive the electrochemical double-layer capacitance (ECSA). Electrochemical impedance spectroscopy (EIS) was conducted at an overpotential of 100 mV in the frequency range between 100 KHz and 0.01 Hz with an AC perturbation of 5 mV. The electrochemical stability was evaluated by chronopotentiometry at a constant current and the potentials with time were recorded.

2.8. Theoretical calculations

The *ab initio* molecular dynamics (AIMD) calculations were performed by CP2K with the Quickstep module [23–25] and semi-empirical GFN1-xTB method. The blank group Co–H_2O as the solid–liquid model included 98 H_2O molecules and 120 Co solid phases. 2 K^+ and 2 OH^- were added to the system to simulate the alkaline environment. In the experimental group, 4 frozen Na^+ were added to the blank group to simulate the power-on state. All the Co atoms except those in the surface layer were frozen. Each model employed first runs of 1000 steps (0.5 picosecond) with a 0.5 fs timestep. EPS_DEFAULT was set to $1.0E^{-10}$ and EPS_SCF of both SCF and OUTER_SCF were set to $1.0E^{-5}$. The temperature was 400 K and the canonical sampling through velocity rescaling (CSVR) method was adopted. The second generation Car-Parrinello molecular dynamics [26] (or called SGMD) was used for 50,000 steps (25 ps) with a 0.5 fs timestep. The NOISY_GAMMA_REGION value was set to $5E^{-7}$ for the Co solid-phase and $2.2E^{-6}$ for the liquid-phase water. MAX_SCF_HIST was set to 6 and the temperature was 400 K.

The density-functional theory (DFT) calculations were performed with CP2K with a cutoff of 400 Ry. In the geometry optimization, the exchange–correlation potential was approximated by the pbe-sol functional based on the generalized gradient approximation, combined with the DZVP-MOLPOT-SR-GTH base set and pseudopotential. The convergence limits were set to $1.0E^{-12}$ for EPS_DEFAULT and $1.0E^{-6}$ for EPS_SCF. A k-point grid of 4 × 4 × 4 was used to sample the first Brillouin zone for MoN. After the geometry optimization, the MoN supercell of 3 × 3 × 1 was built and a 15 Å vacuum layer was introduced along the (002) direction. All the atoms except the surface ones were frozen to be structurally-optimized and to fully relax the surface. The structure was used to construct $Co(OH)_2$-MoN. $Co(OH)_2$-MoN was calculated by the gamma point only with the convergence limits set to $1.0E^{-12}$ for EPS_DEFAULT and $1.0E^{-6}$ for EPS_SCF.

In the energy calculation, the exchange–correlation potential was approximated by the GTH-PBE functional under the generalized gradient approximation in combination with the TZV2P-MOLOPT-SR-GTH base set and pseudopotential. The convergence limits were set to $1.0E^{-14}$ for EPS_DEFAULT and $1.0E^{-7}$ for EPS_SCF. Shermo have calculated the relevant thermodynamic quantities [27]. The Gibbs free energy change (ΔG) in each elementary step was based on the computational hydrogen electrode model as shown by the following equation: $\Delta G = \Delta E + \Delta ZPE - T\Delta S$, where ΔE is obtained directly from the DFT calculation, ΔZPE is the change of zero-point energies (ZPE), T is the temperature of 298.15 K, and ΔS is the change in the entropy of the products and reactants. In the transition state calculation of H_2O^* decomposing into H* and OH* on the catalyst surface, the CI-NEB method was used to insert 10 points between the initial state and final state to find the transition state. The exchange–correlation potential was approximated by the pbe-sol functional under the generalized gradient approximation in combination with the DZVP-MOLPOT-SR-GTH base set and pseudopotential. The convergence limits were set to $1.0E^{-12}$ for EPS_DEFAULT and $1.0E^{-6}$ for EPS_SCF.

3. Results and discussion

3.1. Theoretical verification of crystal facet-induced reconstruction of Co(OH)$_2$

The hydroxylation of Cobalt (Co) in Cobalt-based catalysts under alkaline HER conditions represents a typical cathodic reconstruction process, resulting in the formation of a disordered stack of Co(OH)$_2$ nanosheets on the surface with various crystal facets exposed [28,29] (**Fig. S1**, supporting information). It is well-known that the electrochemical properties of electrocatalysts are closely related to the exposed crystal facets [30,31]. Therefore, the energy of H-OH cleavage for different facet orientations of Co(OH)$_2$ is investigated by DFT calculations. Fig. 1**a** shows that the water dissociation step is hindered on the Co(OH)$_2$ (011), (012), and (100) facets due to the energy barrier. Conversely, this step is exothermic on Co(OH)$_2$ (001) [32], affirming that the (001) facet markedly reduces the barrier for water activation and expedites the kinetics of the Volmer process in alkaline HER [33]. The preferential growth of the Co(OH)$_2$ (001) facet can further enhance the electrocatalytic characteristics. The Platinum-like properties of MoN, good chemical stability, and excellent electron transport capability [34–36] (**Fig. S2-3**) are taken into consideration for Co(OH)$_2$ production. Based on our knowledge of the main exposed surface on MoN from our previous work, MoN (002) is selected to construct the interface model with Co(OH)$_2$ (001). The optimized configuration of Co(OH)$_2$ (001)/MoN (002) is presented in Fig. 1**b**. The lengths of the Co–O and Mo–N bonds are 1.88 Å and 1.90 Å, and the bond angles are 82.64° and 83.73°, respectively. The crystallographic parameters of the two facets are similar, and the interface forming energy is calculated to be −8.46 eV, indicating that the heterointerface is thermodynamically stable [37,38].

As shown in Fig. 1**b–c**, the Mayer bond order of adsorbed hydrogen (H$_{ads}$) on the Co(OH)$_2$ (001)/MoN (002) interface (0.3356) is smaller than that on MoN (002) alone (1.0022), indicating that H$_{ads}$ at the Co(OH)$_2$ (001)/MoN (002) interface can desorb more easily [39]. This inference is further supported by the bond length of M-H$_{ads}$ (M = active site) calculated on both surfaces. When combined with Co(OH)$_2$, the bond length of M-H$_{ads}$ increases by 0.68 Å, demonstrating the lower adsorption energy of H$_{ads}$ [40]. Therefore, as illustrated in Fig. 1**d**, the pre-catalyst comprising metallic Co and MoN used for alkaline HER allows the MoN matrix to function as a preferential template for the directional growth of Co(OH)$_2$ (001), potentially enhancing the overall alkaline electrocatalytic activity.

3.2. Characterizations of the as-synthesized Co–MoN pre-catalyst

According to the theoretical simulation results, the Co–MoN nanoarray pre-catalyst is fabricated on CC by *in situ* thermal nitridation of the hydrothermally prepared $CoMoO_4$ nanoarrays (**Fig. S4**). The XRD pattern matches those of hexagonal MoN [41] (JCPDS No. 25-1367) and metallic Co (JCPDS No. 15-0806) [42] (**Fig. S5**), and the molar ratio of MoN to Co is about 1:0.6 (**Fig. S6** and **Table S1**). The Co–MoN nanoarrays with an average length of 5 μm inherit the quadrangular nanorod structure of $CoMoO_4$. The metallic Co nanodomains with a size of 10 nm are uniformly embedded in the MoN nanoarrays. The interplanar spacings of 2.0 Å, 2.5 Å, and 2.8 Å correspond to the (111) facet of Co [43] as well as (200) and (002) facets of MoN [35], respectively (**Fig. S7**). The mass loading of Co–MoN on CC is calculated to be 8.0 mg cm^{-2} (**Fig. S8**). The BET surface area of Co–MoN nanorod arrays is about 65 ± 15 m^2 g^{-1} which can be attributed to the formation of mesopores resulting from volume shrinkage and phase separation from $CoMoO_4$ to Co–MoN. The pore distribution of Co–MoN nanorod arrays is centered at 3 nm (**Fig. S9**), the abundant mesoporous structure ensures the full contact between electrode materials and electrolyte.

3.3. Dynamic structural evolution of the Co–MoN pre-catalyst

The structural evolution of the Co–MoN pre-catalyst is investigated by electrochemical chronopotentiometry (CP) at a constant current density of 50 mA cm^{-2} in 1 M KOH. As shown in Fig. 2**a**, the Co–MoN electrode exhibits a significant potential drop (≈120 mV) within 5 h, and the optimized HER properties are sustained over an extended period of time. The SEM images disclose an irreversible morphological change of the Co–MoN electrode in the various activation stages (Fig. 2**b**). The quadrangular nanoarrays are covered gradually by hexagonal nanosheets until the electrode stabilizes. To analyze the reason for the morphological changes, *quasi-operando* XRD is performed, as shown in Fig. 2**c**. The self-supporting Co–MoN electrode after activation for 1 h

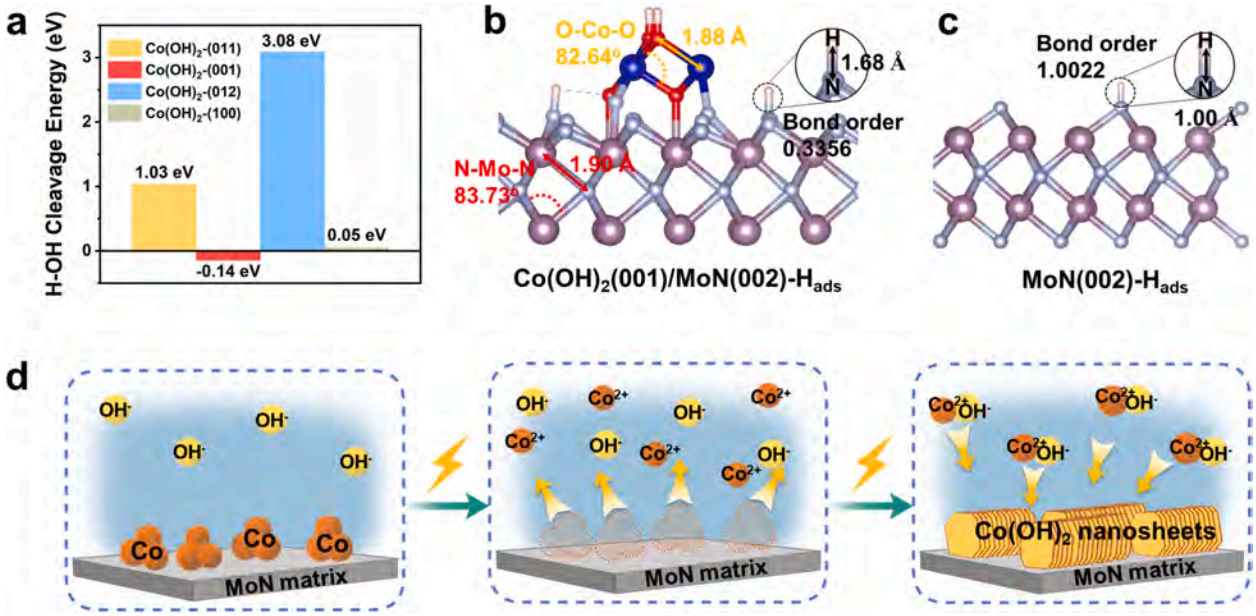

Fig. 1. (a) H-OH cleavage energies on the (011), (001), (012), and (100) facets of Co(OH)$_2$; (b–c) Theoretical model of the Co(OH)$_2$ (001)/MoN (002) heterostructure and MoN (002), including the Mayer order bond and bond length of M-H$_{ads}$; (d) Schematic diagram of the dynamic structural evolution process of the Co–MoN pre-catalyst under alkaline HER conditions.

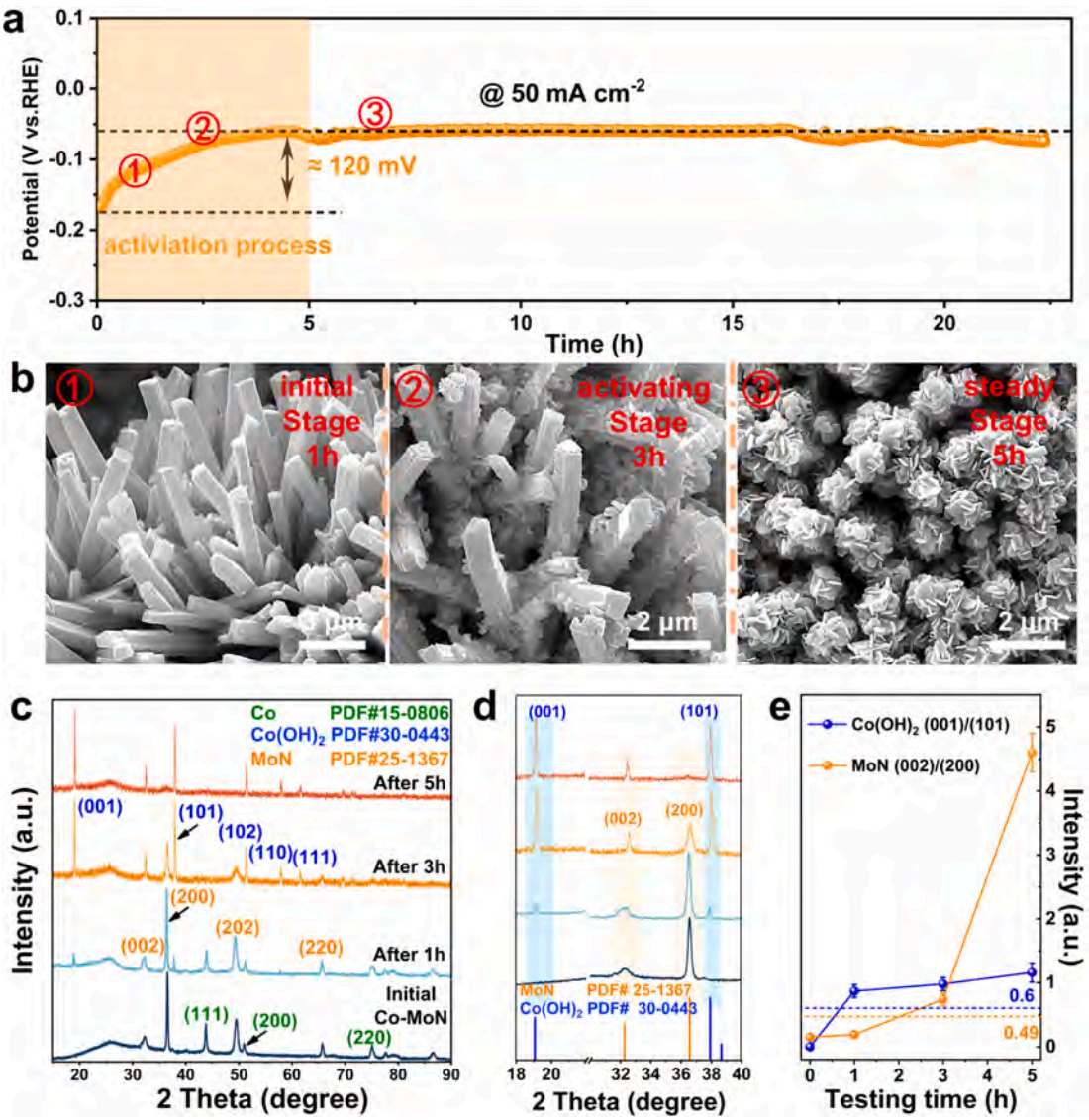

Fig. 2. (a) Chronopotentiometry curve of the Co–MoN electrode at a constant current density of 50 mA in 1 M KOH electrolyte; (b) SEM images and (c) XRD patterns of the Co–MoN electrode at different stages by chronopotentiometry; (d) Magnification of the region between 18° and 40° in Fig. 2c; (e) Changes in the peak intensities of $Co(OH)_2$ (001) and MoN (002), which are normalized by the ratios of $I_{(002)}/I_{(200)}$ in MoN and $I_{(001)}/I_{(101)}$ in $Co(OH)_2$. The error bars are generated from the standard error of the mean derived from three measurements.

exhibits distinctive peaks at 19.1°, 37.9°, 45.0°, 57.9°, and 61.5° corresponding to the (001), (101), (102), (110), and (111) facets of hexagonal $Co(OH)_2$ (JCPDS No. 30-0443) [44], which are not observed from the original sample. Furthermore, as shown in Fig. 2**d**, the MoN (002) and $Co(OH)_2$ (001) facets exhibit a significant enhancement during electrochemical activation. Fig. 2**e** presents the calculated peak intensity ratios of $I_{(002)}/I_{(200)}$ of MoN and $I_{(001)}/I_{(101)}$ of $Co(OH)_2$ after activation. The ratio of $I_{(002)}/I_{(200)}$ of MoN is roughly 10 times larger than the standard value (0.49), and $I_{(001)}/I_{(101)}$ of $Co(OH)_2$ is about twice that of the standard value (0.6). SEM and XRD disclose that the composition and morphology of the Co–MoN electrode have changed dramatically, resulting in a major conversion to the $Co(OH)_2$ (001)/MoN (002) heterostructure after activation for 5 h. Transmission electron microscopy (TEM) is performed to confirm the reconstruction of Co–MoN nanoarrays during alkaline HER (**Fig. S10**). The clear and well-resolved lattice fringes reveal inter-planar spacings of 0.46 nm and 0.25 nm corresponding to the (001) and (002) facets of $Co(OH)_2$ and MoN, respectively [34,45]. The elemental maps validate uniform distributions of the reconstructed components without detectable segregation of metallic Co in the entire region (**Fig. S11**). X-ray photoelectron spectroscopy (XPS) reveals that after the electrochemical activation process, Co^0 peak significantly diminishes, while the peaks associated with Co^{2+} increase [41], indicating the oxidation of metallic Co. Meanwhile, the binding energy position and peak area of MoN remain unchanged, collectively confirming the transformation from Co–MoN to $Co(OH)_2$–MoN (**Fig. S12**).

3.4. Reconstruction mechanism of the Co–MoN pre-catalyst

In order to elucidate the structural evolution mechanism of the Co–MoN pre-catalyst, it is necessary to determine whether analogous changes occur in both the single-phase MoN and Co metal during the alkaline electrochemical test. **Fig. S13** shows the respective multi-step constant current tests of single-phase MoN and metal Co for up to 8 h and reveals no discernible alteration in the voltage required to drive the same current. *Ex situ* XRD reveals that Co is converted to $Co(OH)_2$ to form stacked hexagonal nanosheets (**Fig. S14a–c**). In contrast, the morphology and composition of the single-phase MoN electrode do not change (**Fig. S14d–f**). By comparing Co–MoN and MoN, it can be deduced that the dissolution of Co in the Co–MoN heterostructure

disrupts the original morphology. The remaining MoN tends to expose the crystal facet with the lowest energy to restore the structure stability after Co dissolution. As shown in **Fig. S15**, DFT calculations confirm that the energy of the MoN (002) facet is lower than those of the MoN (200) facet and other facets [37]. Accordingly, the mechanism of the structure and composition evolution of the Co–MoN pre-catalyst is proposed. The metallic Co in Co–MoN undergoes oxidation and dissolution under alkaline HER conditions, and the MoN (002) facet is exposed primarily. Subsequently, MoN (002) serves as the preferential template for the directional growth of $Co(OH)_2$ (001) due to the small lattice mismatch between MoN (002) and $Co(OH)_2$ (001), resulting in the formation of the robust $Co(OH)_2$ (001)/MoN (002) heterointerface. Time-dependent *in situ* Raman scattering is performed to confirm the impact of the alkaline reaction conditions (applied bias and alkaline electrolyte) on the reconstruction process of the Co–MoN pre-catalyst. Fig. 3**a** depicts the *in-situ* Raman spectra of the Co–MoN electrode in 1 M KOH without a bias. The Raman peaks at 815, 844, and 880 cm^{-1} arise from Mo-O vibration modes of MoO_x species on the surface of MoN [46]. After 50 min, new peaks emerge at 460, 515, and 1055 cm^{-1} due to Co–O bending, Co–O symmetrical mode, and OH^- deformation in $Co(OH)_2$ [47,48], signifying the transformation from metallic Co to $Co(OH)_2$. The peaks at 607 and 671 cm^{-1} correspond to the F_{2g} and A_{1g} modes of Co_3O_4 [49]. However, the Co_3O_4 structure is not detected by XRD and XPS, suggesting a partial phase transition from Co to Co_3O_4 due to laser heating during the Raman experiment [50]. To analyze the influence of the applied bias, *in situ* Raman spectra are obtained from Co–MoN in 1 M KOH at −0.02 V and −0.05 V *vs.* Ag/AgCl, respectively, and the results are resented in Fig. 3**b–c**. When a more negative bias is applied, the same signals of $Co(OH)_2$ appear in a shorter period of time, as shown in Fig. 3**a**. The comparison of normalized intensities for the Co–O bending mode in Fig. 3**d** reveals that hydroxylation of metallic cobalt progresses slowly and spontaneously. However, increasing the applied bias expedites this process. The same test is conducted in deionized water, and no Raman signal is detected from $Co(OH)_2$ during the entire 60-minute test (**Fig. S16**), indicating that an alkaline environment is necessary for the cathodic reconstruction. *Ab initio* molecular dynamics (AIMD) simulations are conducted to investigate the mechanism of oxidation and dissolution of metallic Co under reduction conditions. As shown in Fig. 3**e** and **Video S1-2** in supporting information, upon the application of a bias voltage, the electric field drives the movement of H^+ toward Co, and the repulsive effect caused by proton permeating into the metal increases the susceptibility of the outermost Co atoms to dissolution within 25 fs [51]. The Co atoms from the second outer layer then become the new outer layer and undergo a similar interaction with H^+. This cycle perpetuates resulting in the complete dissolution of Co. However, in the absence of a bias, it is difficult for H^+ at the solid–liquid interface to enter the inter-lattice space of Co, which remains stable throughout the entire 25-picosecond simulation period (**Fig. S17**). The concentration of Co^{2+} in the electrolyte is determined by inductively-coupled plasma mass spectrometry (ICP-MS) and CP test (Fig. 3**f**) [52].

The Co^{2+} concentration is consistently low throughout the process without an applied bias. Conversely, the Co^{2+} concentration increases with time in the presence of an externally applied bias, reaching the peak after 2.5 h and then decreasing to a lower level. This temporal pattern corresponds to the activation process observed from the CP curves (in Fig. 2a) and confirms the dynamic process involving the dissolution of metallic Co and subsequent re-growth of $Co(OH)_2$. In general, the applied bias acts as the driving force to accelerate the

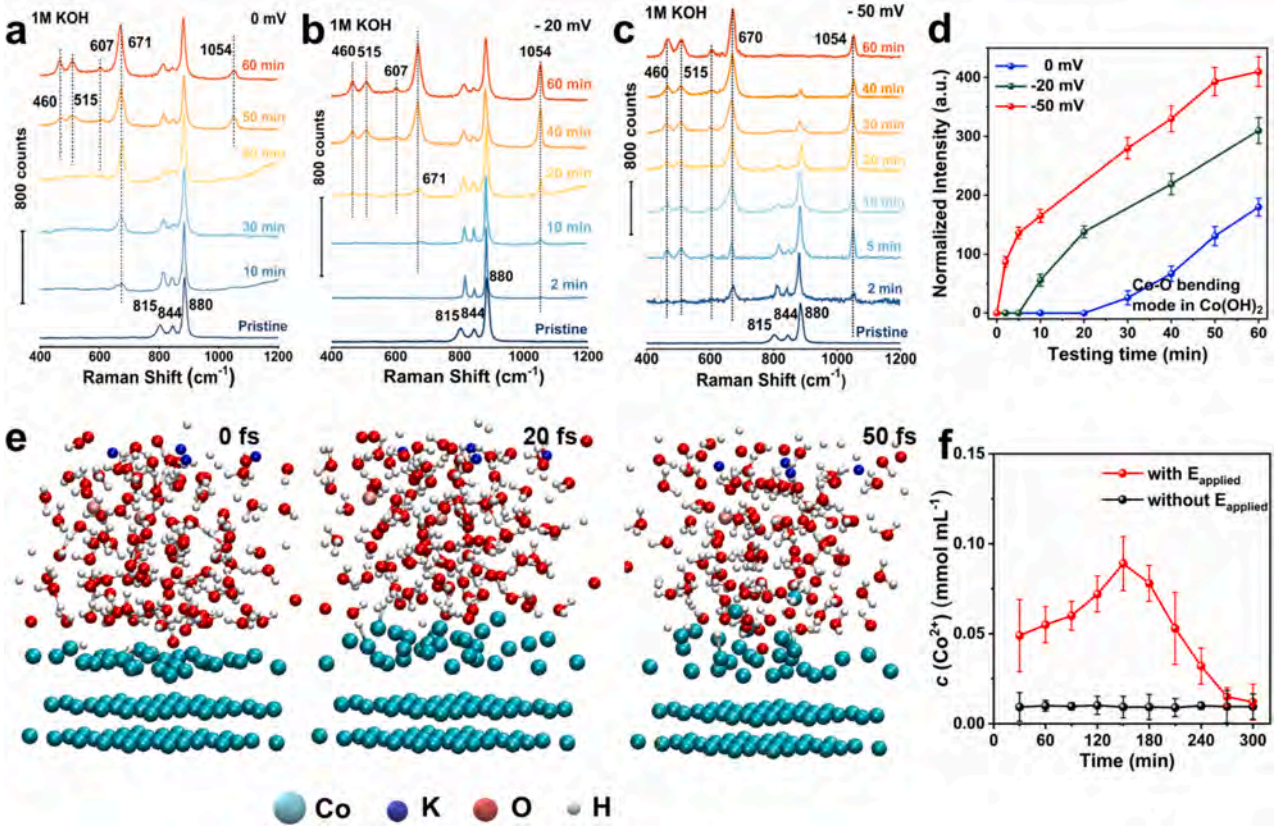

Fig. 3. Time-dependent *in situ* Raman scattering spectra of the Co–MoN pre-catalyst: (a) 1 M KOH with 0 V applied; (b) 1 M KOH with −0.02 V (*vs.* Ag/AgCl) applied; (c) 1 M KOH with −0.05 V (*vs.* Ag/AgCl) applied; (d) Comparison of normalized intensities for the Co–O bending mode; (e) Snapshots taken in the classical molecular dynamics simulations of the cobalt metal-electrolyte (1 M KOH) system on the electrode surface: With the applied bias at 0, 20 and 50 fs; (f) Time-dependent Co^{2+} concentrations in the electrolyte leached from the Co–MoN pre-catalyst with and without the applied bias. The error bars are generated from the standard error of the mean derived from three measurements.

dissolution and oxidation of metallic Co in the reducing environment, while the electrolyte plays a crucial role in supplying the essential reactants and establishing the environment conducive to mass and charge transfer [53]. These two factors collectively initiate the cathodic reconstruction process.

3.5. Dynamic activity variation of the Co–MoN pre-catalyst

Linear scan voltammetry (LSV) is conducted on the Co–MoN pre-catalyst for 14 cycles from −0.9 to −1.5 V *vs.* Hg/HgO at a scanning rate of 0.4 mV s^{-1} in 1 M KOH (**Fig. S18**). The 3rd, 7th, and 12th cycles correspond to 1 h, 3 h, and 5 h in the CP test in Fig. 2a, respectively. Fig. 4**a** demonstrates that the overpotentials decrease with successive LSV scans. The overpotential for driving 100 mA cm^{-2} current density stabilizes following a decrease of approximately 120 mV (58 % potential drop), resulting in an ultra-low overpotential of 86 mV at 100 mA cm^{-2} after the 12th cycle. This value is slightly better than that of Pt/C (99 mV) and significantly lower than those of MoN (310 mV) and metallic Co (480 mV). Moreover, the post-activated Co–MoN electrode has better electrocatalytic activity than Pt/C at ampere-level current densities for the same mass loading (Fig. 4**b**). The Tafel slopes decrease with the LSV curve from the 1st, 3rd, 7th, and 12th cycles (Fig. 4**c**), demonstrating that the reaction is continuously accelerated throughout reconstruction. Specifically, the result of the 12th LSV curve (42.5 mV dec^{-1}) is 24.5 % lower than that of the first curve (56.3 mV dec^{-1}), indicating the Co–MoN pre-catalyst follows the Volmer-Heyrovsky process: $H_2O + e^- \rightarrow H^* + OH^-$ (Volmer Step) and $H^* + H_2O + e^- \rightarrow OH^- + H_2$ (Heyrovsky Step) [54]. The consecutive electrochemical impedance spectroscopy (EIS) plots are recorded for HER, and a continuous decline in the charge transfer resistance (R_{ct}) is observed. The R_{ct} of 3.75 Ω after the 12th cycle is 70 % of the initial value (5.4 Ω) (Fig. 4**d**). The electrochemical active surface area (ECSA) is an important parameter to evaluate the exposed active sites, which are associated with the double-layer capacitance (C_{dl}) measured by cyclic voltammetry (CV) at different scanning rates in the non-Faradaic potential range of 0.1–0.2 V *vs.* Hg/HgO (**Fig. S19**). The C_{dl} value of the Co–MoN pre-catalyst is determined after each LSV test and the C_{dl} value increases by 1.2 times, revealing that more active sites are exposed as the reconstruction progresses (Fig. 4**e**). To evaluate the changes in intrinsic activity of the Co–MoN during the reconstruction process, the LSV curves are normalized by the ECSA. As shown in **Fig. S20**, as the reconstruction process progresses, the reconstructed electrode demonstrates an increasing intrinsic activity. This enhancement can be attributed to the greater exposure of the MoN (002) facet resulting from Co dissolution and the formation of abundant $Co(OH)_2$ (001)-MoN (002) heterointerface. The turnover frequency (TOF) of the reconstructed $Co(OH)_2$-MoN is much higher than

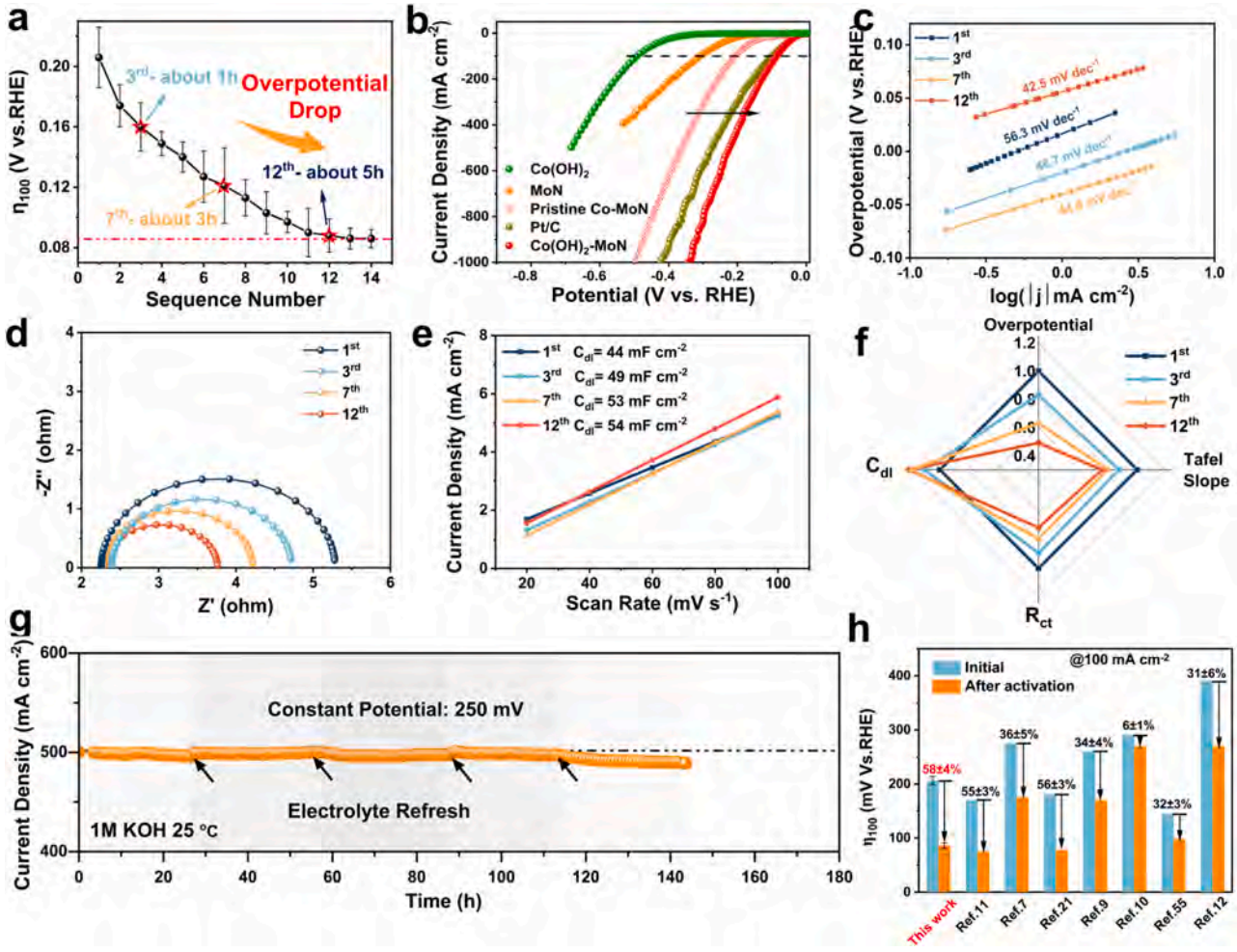

Fig. 4. (a) Consecutive LSV curves of the Co–MoN pre-catalyst for 14 cycles, revealing the overpotential decrease with cycles and then stabilize after the 12th cycle; (b) Comparison of the LSV curves of the reconstructed $Co(OH)_2$-MoN, pristine Co–MoN, Pt/C, $Co(OH)_2$, and single-phase MoN; (c) Tafel slopes, (d) EIS plots, and (e) Double-layer capacitance (C_{dl}) corresponding to the consecutive LSV curves; (f) Comparison of the overpotentials, Tafel slopes, R_{ct} and C_{dl} of the 1st, 3rd, 7th, and 12th cycles; (g) Evaluation of the reconstructed $Co(OH)_2$-MoN stability by chronoamperometry method; (h) Comparing the performance self-optimization degree with other Co-based catalysts by using the change in overpotential at 100 mA cm^{-2} as the standard. The error bars are generated from the standard error of the mean derived from three measurements.

that of commercial Pt/C, further corroborating the high intrinsic catalytic activity in alkaline media (Fig. S21). The comparison of the overpotentials, Tafel slopes, and R_{ct} and C_{dl} of the 1st, 3rd, 7th, and 12th cycles are shown in Fig. 4**f**. It is evident that the induced reconstruction enhances the intrinsic HER catalytic activity, accelerates charge and mass transfer, and exposes more active sites for H_{ad} conversion. Subsequently, an acid-soaking experiment is conducted to investigate the roles of $Co(OH)_2$ and MoN in catalyzing alkaline HER. As shown in Fig. S22, after immersion in a 0.5 M HCl solution for a specified duration, the nanorod structure is retained, but the surface becomes rough after the removal of the $Co(OH)_2$ nanosheets. XRD confirms that the only remaining compound is MoN which still exhibits an abnormal enhancement of the (002) facet orientation (Fig. S23a). LSV shows a decline in the catalytic activity on the reconstructed electrode with increased pickling time after the removal of $Co(OH)_2$. However, the remaining MoN still exhibits enhanced hydrogen evolution activity (175 mV @100 mA cm^{-2}) compared to the pure MoN (310 mV@100 mA cm^{-2}) (Fig. S23b), indicating that the intrinsic catalytic activity of MoN (002) is superior to that of other facets. Therefore, we speculate that the increasing $Co(OH)_2$ (001) nanosheets mainly act as water dissociation sites, while MoN (002) is active for H_{ad} adsorption/desorption. The continuous HER stability of the reconstructed $Co(OH)_2$-MoN electrode is assessed by chronoamperometry and CV tests (Fig. 4**g** and Fig. S24). Benefiting from the robust coupled heterointerface, the reconstructed electrode shows high durability at a high current density of 0.5 A cm^{-2} in 1 M KOH for over 110 h. Additionally, the XRD and SEM analyses of the catalyst after stability tests are provided in Fig. S24b-d. These results indicate that the reconstructed $Co(OH)_2$-MoN catalyst maintains its structural and composition integrity over extended use, highlighting its promising long-term performance for practical applications. The self-optimization degree from the reconstruction of Co–MoN with other Co-based reconstructed catalysts is evaluated based on the change in overpotential at 100 mA cm^{-2} as the standard (Fig. 4**h**). Clearly, owing to the directional induced reconstruction, $Co(OH)_2$-MoN shows a 58 ± 4 % overpotential drop, which is superior to other reported work [45,55] and demonstrates the superiority of modulating the exposed crystal faces of the reconstructed phase. The faradic efficiency (FE) of the reconstructed $Co(OH)_2$-MoN electrode during HER process is assessed in a three-electrode system under the constant current (0.1 A) for 6 h and the FE can be sustained over 95 % (Fig. S25).

3.6. *Theoretical assessment of the reconstructed $Co(OH)_2$ (001)/MoN (002)*

DFT calculations are conducted to further elucidate the relationship between the reconstructed structure and the enhanced electrocatalytic activity of the $Co(OH)_2$ (001)/MoN (002) heterointerface. The results in Fig. 4c indicate that the HER process on the $Co(OH)_2$-MoN

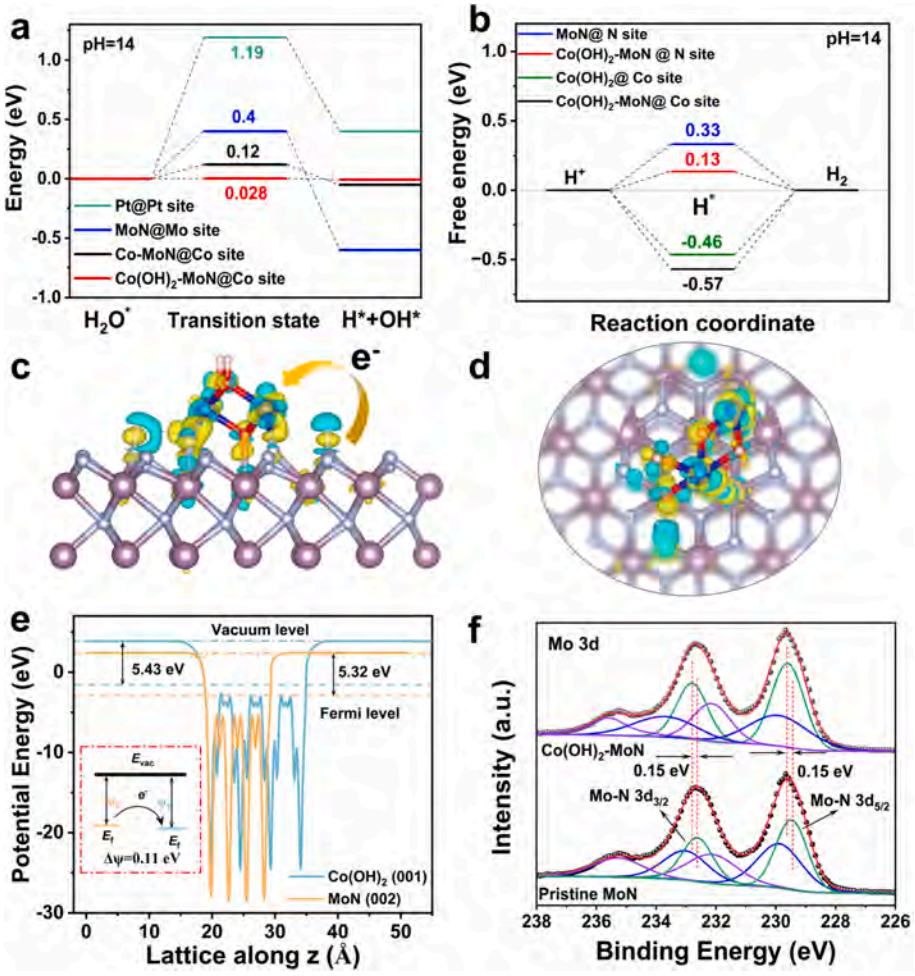

Fig. 5. (a) Energy profiles of water dissociation for commercial Pt, MoN, Co–MoN, $Co(OH)_2$-MoN; (b) Free energy diagrams of alkaline HER on different sites for MoN, $Co(OH)_2$, and reconstructed $Co(OH)_2$-MoN; Charge density difference plot at the $Co(OH)_2$-MoN interface: (c) Side view and (d) Top view, yellow and blue isosurfaces representing electron accumulation and electron depletion; (e) Work functions of $Co(OH)_2$ (001) and MoN (002), E_{vac}, E_f, $\Delta\psi$ represent the vacuum level, Fermi level and work function difference, respectively; (f) High-resolution XPS spectra of Mo 3*d* obtained from MoN and reconstructed $Co(OH)_2$-MoN. (For interpretation of the references to colour in this figure legend, the reader is referred to the web version of this article.)

electrocatalyst follows Volmer-Heyrovsky reactions. Therefore, the water dissociation and H_{ads} desorption steps of $Co(OH)_2$-MoN should be evaluated. The Gibbs free energy for water dissociation on MoN, Co–MoN, $Co(OH)_2$-MoN, and Pt are calculated (Fig. 5**a**). Consistent with previous works, the high energy barrier of Pt (1.19 eV) for water dissociation significantly hinders alkaline HER. In comparison, the values for MoN (0.4 eV), Co–MoN (0.12 eV), and $Co(OH)_2$ (001)/MoN (002) (0.028 eV) suggest that coupling $Co(OH)_2$ with MoN accelerates water dissociation to facilitate the formation of the hydrogen intermediate (H*) with an extremely low energy barrier in alkaline HER [12,56,57]. Moreover, the free energies of hydrogen adsorption (ΔG_{H^*}) of individual sites in different systems are compared in Fig. 5**b**. Relative to MoN (0.33 eV- N site), ΔG_{H^*} of the N site (0.13 eV) on $Co(OH)_2$ (001)/MoN (002) is more neutral, indicating optimized hydrogen interactions for higher HER activity [58]. Furthermore, the Co site of the heterointerface exhibits stronger proton aggregation ability (−0.57 eV) than the pure $Co(OH)_2$ surface (−0.46 eV). This is likely due to electron transfer at the interface. Fig. 5**c–d** presents the charge density difference to evaluate the accurate charge distribution of the heterointerface. It is shown that MoN at the interface donates electrons to the adjacent $Co(OH)_2$, giving rise to the local acidic proton-rich environment [59]. Fig. 5**e**. It shows an overall transfer from MoN (002) to $Co(OH)_2$ (001), with a small $\Delta\psi$ of 0.11 eV between them. This small $\Delta\psi$ barrier reduces charge accumulation and proton capture at the interface, thus facilitating the migration of H* from the water dissociation site to the H* desorption site [60,61].

The work function difference ($\Delta\psi$) between $Co(OH)_2$ (001) and MoN (002) is evaluated in The interface charge interaction is further confirmed by XPS. As shown in Fig. 5**f**, the binding energy of Mo-N in the $Co(OH)_2$ (001)/MoN (002) heterostructure shows a positive shift of 0.15 eV compared to that in MoN alone, suggesting electron transfer from MoN to adjacent $Co(OH)_2$ [36]. Therefore, the catalytic mechanism for the reconstructed $Co(OH)_2$ (001)/MoN (002) in alkaline media *via* the synergy of multi-function catalytic sites is proposed. The $Co(OH)_2$ (001) facet facilitates water dissociation and generates abundant H*. The heterointerface acts as the channel for H* migration, and the MoN (002) facet exhibits an optimized hydrogen adsorption energy (ΔG_{H^*}) for fast H* adsorption/desorption. Collectively, these factors contribute to the enhanced alkaline HER performance.

4. Conclusions

In this study, we systematically investigate the time- and potential-dependent structural and compositional transformation of Co–MoN pre-catalyst under alkaline HER conditions. Our findings reveal that the MoN (002) facet plays a crucial role in preferentially inducing the transformation of metallic Co to $Co(OH)_2$ (001) in a reducing environment. This transformation leads to the formation of abundant $Co(OH)_2$ (001)/MoN (002) heterostructure that continuously enhances HER performance, achieving a significant 58 % reduction in overpotential. Theoretical calculations indicate that the optimal $Co(OH)_2$ (001) facet minimizes the water dissociation barrier and modulates the electronic structure of MoN (002) through interfacial interactions, thereby promoting intrinsic HER activity. The post-activated $Co(OH)_2$-MoN electrode delivers remarkable performance, with low overpotentials of 86 mV@100 mA cm^{-2} and 339 mV@1 A cm^{-2}, along with stability during continuous electrolysis over 110 h. Our study introduces an innovative pre-catalyst design strategy, wherein the desired active surface is induced through reconstruction to enhance catalytic performance. Unlike previous studies that focused on static catalyst configurations, our approach emphasizes the role of dynamic structural evolution in optimizing catalytic efficiency for alkaline HER. Moving forward, future research should focus on further tuning the $Co(OH)_2$-MoN interface and deepening our understanding of its long-term stability and scalability for industrial applications. Moreover, applying this approach to other transition metal-based pre-catalysts could provide valuable insights into the design of highly efficient and durable catalysts for sustainable energy technologies.

CRediT authorship contribution statement

Chaoran Pi: Writing – original draft, Visualization, Methodology, Data curation, Conceptualization. **Difei Leng:** Visualization, Investigation, Data curation. **Xuming Zhang:** Writing – review & editing, Visualization, Funding acquisition. **Shuangjie Wu:** Funding acquisition. **Yun Li:** Funding acquisition. **Li Huang:** Funding acquisition. **Zhihong Liu:** Visualization, Methodology. **Paul K. Chu:** Writing – review & editing, Visualization, Funding acquisition. **Kaifu Huo:** Writing – review & editing, Visualization, Supervision, Project administration, Funding acquisition, Conceptualization.

Declaration of competing interest

The authors declare that they have no known competing financial interests or personal relationships that could have appeared to influence the work reported in this paper.

Acknowledgements

The authors gratefully acknowledge the financial support provided by the National Natural Science Foundation of China (U2004210 and 22379116), Basic Research Program of Shenzhen Municipal Science and Technology Innovation Committee (JCYJ20230807143612026, JCYJ20210324141613032), and City University of Hong Kong Donation Research Grants (DON-RMG 9229021 and 9220061).

Appendix A. Supplementary data

Supplementary data to this article can be found online at https://doi.org/10.1016/j.jcis.2025.02.066.

Data availability

Data will be made available on request.

References

[1] M. Chatenet, B. Pollet, D. Dekel, F. Dionigi, J. Deseure, P. Millet, R. Braatz, M. Bazant, M. Eikerling, I. Water electrolysis: from textbook knowledge to the latest scientific strategies and industrial developments, *Chem. Soc. Rev.* 51 (11) (2022) 4583–4762.
[2] A. Shah, Z. Zhang, Z. Huang, S. Wang, G. Zhong, C. Wan, A. Alexandrova, Y. Huang, X. Duan, The role of alkali metal cations and platinum-surface hydroxyl in the alkaline hydrogen evolution reaction, *Nat. Catal.* 5 (10) (2022) 923–933.
[3] H. Hu, X. Wang, Z. Zhang, J. Liu, X. Yan, X. Wang, J. Wang, J. Attfield, M. Yang, Engineered nickel-iron nitride electrocatalyst for industrial-scale seawater hydrogen production, *Adv. Mater.* (2024) e2415421.
[4] R. Liu, M. Sun, X. Liu, Z. Lv, X. Yu, J. Wang, Y. Liu, L. Li, X. Feng, W. Yang, Enhanced metal-support interactions boost the electrocatalytic water splitting of supported ruthenium nanoparticles on a Ni_3N/NiO heterojunction at industrial current density, *Angew. Chem.* 135 (46) (2023) e202312644.
[5] X. Li, Z. Huang, C. Shuck, G. Liang, Y. Gogotsi, C. Zhi, MXene chemistry, electrochemistry and energy storage applications, *Nat. Rev. Chem.* 6 (2022) 389–404.
[6] S. Anantharaj, S. Ede, K. Sakthikumar, K. Karthick, S. Mishra, S. Kundu, Recent trends and perspectives in electrochemical water splitting with an emphasis on sulfide, selenide, and phosphide catalysts of Fe, Co, and Ni: a review, *ACS Catal.* 6 (12) (2016) 8069–8097.
[7] P. Ji, R. Yu, P. Wang, X. Pan, H. Jin, D. Zheng, D. Chen, J. Zhu, Z. Pu, J. Wu, Ultrafast and in-depth reconstruction of transition metal fluorides in electrocatalytic hydrogen evolution processes, *Adv. Sci.* 9 (3) (2022) 2103567.
[8] X. Luo, X. Tan, P. Ji, L. Chen, J. Yu, S. Mu, Surface reconstruction-derived heterostructures for electrochemical water splitting, *EnergyChem* 5 (2) (2023) 100091.
[9] Y. Sun, J. Wu, Z. Zhang, Q. Liao, S. Zhang, X. Wang, Y. Xie, K. Ma, Z. Kang, Y. Zhang, Phase reconfiguration of multivalent nickel sulfides in hydrogen evolution, *Energ. Environ. Sci.* 15 (2) (2022) 633–644.

[10] F. Wu, R. Yang, S. Lu, W. Du, B. Zhang, Y. Shi, Unveiling partial transformation and activity origin of sulfur vacancies for hydrogen evolution, *ACS Energy Lett.* 7 (12) (2022) 4198–4203.

[11] L. Wang, Y. Hao, L. Deng, F. Hu, S. Zhao, L. Li, S. Peng, Rapid complete reconfiguration induced actual active species for industrial hydrogen evolution reaction, *Nat. Commun.* 13 (1) (2022) 5785.

[12] L. Jiang, Y. Huang, Y. Zou, C. Meng, Y. Xiao, H. Liu, J. Wang, Boosting the stability of oxygen vacancies in α-$Co(OH)_2$ nanosheets with coordination polyhedrons as rivets for high-performance alkaline hydrogen evolution electrocatalyst, *Adv. Energy Mater.* 12 (43) (2022) 2202351.

[13] H. Su, S. Song, Y. Gao, N. Li, Y. Fu, L. Ge, W. Song, J. Liu, T. Ma, In situ electronic redistribution tuning of $NiCo_2S_4$ nanosheets for enhanced electrocatalysis, *Adv. Funct. Mater.* 32 (14) (2022) 2109731.

[14] C. Yang, W. Zhong, K. Shen, Q. Zhang, R. Zhao, H. Xiang, Electrochemically reconstructed Cu-FeOOH/Fe_3O_4 catalyst for efficient hydrogen evolution in alkaline media, *Adv. Energy Mater.* 12 (16) (2022) 2200077.

[15] L. Su, X. Cui, T. He, L. Zeng, H. Tian, Y. Song, K. Qi, B.Y. Xia, Surface reconstruction of cobalt phosphide nanosheets by electrochemical activation for enhanced hydrogen evolution in alkaline solution, *Chem. Sci.* 10 (7) (2019) 1–9.

[16] F. Li, C. Xia, B. Xia, Exploration and insight of dynamic structure evolution for electrocatalysts, *Acc. Mater. Res.* 4 (5) (2023) 427–437.

[17] F. Li, L. Huang, S. Zaman, W. Guo, H. Liu, X. Guo, B. Xia, Corrosion chemistry of electrocatalysts, *Adv. Mater.* 34 (52) (2022) 2200840.

[18] H. Liao, G. Ni, P. Tan, K. Liu, X. Liu, H. Liu, K. Chen, X. Zheng, M. Liu, J. Pan, Oxyanion engineering suppressed iron segregation in nickel-iron catalysts toward stable water oxidation, *Adv. Mater.* 35 (21) (2023) 2300347.

[19] J. Feng, X. Wang, H. Pan, In-situ reconstruction of catalyst in electrocatalysis, *Adv. Mater.* (2024) 2411688.

[20] W. Zhang, Y. Yang, Y. Tang, Q. Gao, In-situ reconstruction of catalysts in cathodic electrocatalysis: new insights into active-site structures and working mechanisms, *J. Energy Chem.* 70 (2022) 414–436.

[21] L. Deng, S. Hung, S. Zhao, W. Zeng, Z. Lin, F. Hu, Y. Xie, L. Yin, L. Li, S. Peng, Unveiling coordination transformation for dynamically enhanced hydrogen evolution catalysis, *Energ. Environ. Sci.* 16 (11) (2023) 5220–5230.

[22] L. Xia, X. Zhang, H. Song, Y. Zheng, X. Li, B. Gao, K. Huo, P.K. Chu, Structural engineering of hierarchically hetestructured Mo_2C/Co conformally embedded in carbon for efficient water splitting, *Int. J. Hydrogen Energy* 45 (43) (2020) 22629–22637.

[23] T. Kühne, M. Iannuzzi, M. Ben, V. Rybkin, P. Seewald, F. Stein, T. Laino, R. Khaliullin, O. Schütt, F. Schiffmann, CP2K: An electronic structure and molecular dynamics software package-quickstep: efficient and accurate electronic structure calculations, *J. Chem. Phys.*, 152 (2020) 194103.

[24] S. Grimme, S. Ehrlich, L. Goerigk, Effect of the damping function in dispersion corrected density functional theory, *J. Comput. Chem.*., 32 (2011) 1456–1465.

[25] S. Grimme, J. Antony, S. Ehrlich, H. Krieg, A consistent and accurate ab initio parametrization of density functional dispersion correction (DFT-D) for the 94 elements H-Pu, *J. Chem. Phys.* 132 (2010) 154104.

[26] T.D. Kühne, Second generation car-parrinello molecular dynamics, *WIREs Comput. Mol. Sci.* 4 (2014) 391–406.

[27] T. Lu, Q. Chen, Shermo: A general code for calculating molecular thermochemistry properties, *Comput. Theor. Chem.* 1200 (2021) 113249.

[28] L. Qiao, D. Liu, A. Zhu, J. Feng, P. Zhou, C. Liu, K. Ng, H. Pan, Nickel-facilitated in-situ surface reconstruction on spinel Co_3O_4 for enhanced electrochemical nitrate reduction to ammonia, *Appl. Catal. B: Environ.* 340 (2024) 123219.

[29] L. Qiao, A. Zhu, D. Liu, K. An, J. Feng, C. Liu, K.W. Ng, H. Pan, In situ reconstructed Cu/β-$Co(OH)_2$ tandem catalyst for enhanced nitrate electroreduction to ammonia in ampere-level, *Adv. Energy Mater.* (2024), 2402805.

[30] Y. Hong, S. Dutta, S. Jang, O. Ngome Okello, H. Im, S. Choi, J. Han, I. Lee, Crystal facet-manipulated 2D Pt nanodendrites to achieve an intimate heterointerface for hydrogen evolution reactions, *J. Am. Chem. Soc.* 144 (20) (2022) 9033–9043.

[31] A. Zhu, H. Liu, S. Bu, K. Liu, C. Luan, D. Lin, G. Gan, Y. Zhou, T. Zhang, K. Liu, Facet-dependent evolution of active components on spinel Co_3O_4 for electrochemical ammonia synthesis, *ACS Nano* 18 (33) (2024) 22344–22355.

[32] X. Chen, X. Wang, J. Le, S. Li, X. Wang, Y. Zhang, P. Radjenovic, Y. Zhao, Y. Wang, X. Lin, Revealing the role of interfacial water and key intermediates at ruthenium surfaces in the alkaline hydrogen evolution reaction, *Nat. Commun.* 14 (1) (2023) 5289.

[33] Z. Zeng, K. Chang, J. Kubal, N. Markovic, J. Greeley, Stabilization of ultrathin (hydroxy) oxide films on transition metal substrates for electrochemical energy conversion, *Nat. Energy* 2 (6) (2017) 1–9.

[34] X. Luo, H. Song, Y. Ren, X. Zhang, K. Huo, P.K. Chu, In-plane heterostructured MoN/Mo_2N nanosheets as high-efficiency electrocatalysts for alkaline hydrogen evolution reaction, *APL Mater.* 11 (6) (2023).

[35] D. Gao, S. Deng, X. Li, Y. Zhang, T. Lv, Y. He, W. Mao, H. Yang, J. Zhang, P.K. Chu, Lithiophilic and conductive framework of 2D MoN nanosheets enabling planar lithium plating for dendritefree and minimum-volume-change lithium metal anodes, *Chem. Eng. J.* 454 (2023) 140144.

[36] C. Pi, X. Li, X. Zhang, H. Song, Y. Zheng, B. Gao, A. Kızılaslan, P.K. Chu, K. Huo, In-plane Mott-Schottky effects enabling efficient hydrogen evolution from Mo_5N_6-MoS_2 heterojunction nanosheets in universal-pH electrolytes, *Small* 18 (22) (2022) 2201137.

[37] H. Zhang, Y. Zhong, J. Li, Y. Liao, J. Zeng, Y. Shen, L. Yuan, Z. Li, Y. Huang, Inducing the preferential growth of Zn (002) plane for long cycle aqueous Zn-ion batteries, *Adv. Energy Mater.* 13 (1) (2023) 2203254.

[38] D. Liu, X. Wei, J. Lu, X. Wang, K. Liu, Y. Cai, Y. Qi, L. Wang, H. Ai, Z. Wang, Efficient and ultrastable seawater electrolysis at industrial current density with strong metal-support interaction and dual Cl–repelling layers, *Adv. Mater.* (2024) 2408982.

[39] J. Du, J. Hurd, J. Seed, G. Balázs, M. Scheer, R. Adams, D. Lee, S. Liddle, 31P nuclear magnetic resonance spectroscopy as a probe of thorium-phosphorus bond covalency: correlating phosphorus chemical shift to metal-phosphorus bond order, *J. Am. Chem. Soc.* 145 (40) (2023) 21766–21784.

[40] C. Cai, K. Liu, L. Zhang, F. Li, Y. Tan, P. Li, Y. Wang, M. Wang, Z. Feng, D. Motta Meira, Atomically local electric field induced interface water reorientation for alkaline hydrogen evolution reaction, *Angew. Chem. Int. Ed.* 62 (26) (2023) e202300873.

[41] J. Sun, W. Xu, C. Lv, L. Zhang, M. Shakouri, Y. Peng, Q. Wang, X. Yang, D. Yuan, M. Huang, Co/MoN hetero-interface nanoflake array with enhanced water dissociation capability achieves the Pt-like hydrogen evolution catalytic performance, *Appl. Catal. B: Environ.* 286 (2021) 119882.

[42] X. Lang, M. Qadeer, G. Shen, R. Zhang, S. Yang, J. An, L. Pan, J. Zou, A Co-Mo_2N composite on a nitrogen-doped carbon matrix with hydrogen evolution activity comparable to that of Pt/C in alkaline media, *J. Mater. Chem. A* 7 (36) (2019) 20579–20583.

[43] T. Xiong, X. Yao, Z. Zhu, R. Xiao, Y. Hu, Y. Huang, S. Zhang, M. Balogun, In situ grown co-based interstitial compounds: non-3d metal and non-metal dual modulation boosts alkaline and acidic hydrogen electrocatalysis, *Small* 18 (9) (2022) 2105331.

[44] K. Guo, Y. Wang, J. Huang, M. Lu, H. Li, Y. Peng, P. Xi, H. Zhang, J. Huang, S. Lu, In situ activated Co_{3-x} Ni_xO_4 as a highly active and ultrastable electrocatalyst for hydrogen generation, *ACS Catal.* 11 (13) (2021) 8174–8182.

[45] K. Fan, L. Zong, J. Liu, C.H. Chuang, M. Dong, Y. Zou, Y. Xu, H.Q. Fu, L. Zhang, L. Wang, In situ reconstruction to surface sulfide adsorbed metal scaffold for enhanced electrocatalytic hydrogen evolution activity, *Adv. Energy Mater.* (2024) 2400052.

[46] C. Williams, J. Ekerdt, J. Jehng, F. Hardcastle, A. Turek, I. Wachs, A Raman and ultraviolet diffuse reflectance spectroscopic investigation of silica-supported molybdenum oxide, *J. Phy. Chem.* 95 (22) (1991) 8781–8791.

[47] O. Bøckman, T. Østvold, G. Voyiatzis, G. Papatheodorou, Raman spectroscopy of cemented cobalt on zinc substrates, *Hydrometallurgy* 55 (1) (2000) 93–105.

[48] J. Yang, H. Liu, W.N. Martens, R.L. Frost, Synthesis and characterization of cobalt hydroxide, cobalt oxyhydroxide, and cobalt oxide nanodiscs, *J. Phy. Chem. C* 114 (1) (2010) 111–119.

[49] Q. Quan, X. Bu, D. Chen, F. Wang, X. Kang, W. Wang, Y. Meng, S. Yip, C. Liu, J. Ho, Sequential self-reconstruction of localized Mo species in hierarchical carbon/Co–Mo oxide heterostructures for boosting alkaline hydrogen evolution kinetics and durability, *J. Mater. Chem. A* 10 (8) (2022) 3953–3962.

[50] W. Zheng, M. Liu, L.Y.S. Lee, Electrochemical instability of metal–organic frameworks: in situ spectroelectrochemical investigation of the real active sites, *ACS Catal.* 10 (1) (2019) 81–92.

[51] Y. Li, H. Pan, Q. Liu, X. Ming, Z. Li, Ab initio mechanism revealing for tricalcium silicate dissolution, *Nat. Commun.* 13 (1) (2022) 1253.

[52] W. Du, Y. Shi, W. Zhou, Y. Yu, B. Zhang, Unveiling the in-situ dissolution and polymerization of Mo in Ni_4Mo alloy for promoting the hydrogen evolution reaction, *Angew. Chem. Int. Ed.* 60 (13) (2021) 7051–7055.

[53] Y. Zeng, M. Zhao, Z. Huang, W. Zhu, J. Zheng, Q. Jiang, Z. Wang, H. Liang, Surface reconstruction of water splitting rlectrocatalysts, Adv. Energy Mater. 12 (33) (2022) 2201713.

[54] W. Zhai, Y. Ma, D. Chen, J.C. Ho, Z. Dai, Y. Qu, Recent progress on the long-term stability of hydrogen evolution reaction electrocatalysts, InfoMat 4 (9) (2022) e12357.

[55] X. Yu, Y. Chen, Y. Wu, X. Chu, B. Liu, B. Hu, G. Che, W. Jiang, C. Liu, Self-reconstructed ZIF-L/$Co(OH)_2$ heterointerface modulates electronic structure of Ru and boosts electrocatalytic hydrogen evolution, *Chem. Eng. J.* 490 (2024) 151926.

[56] X. Li, N. Li, Z. Huang, Z. Chen, G. Liang, Q. Yang, M. Li, Y. Zhao, L. Ma, B. Dong, Enhanced redox kinetics and duration of aqueous I_2/I^- conversion chemistry by MXene confinement, Adv. Mater. 33 (2021) 2006897.

[57] X. Li, N. Li, Z. Huang, Z. Chen, Y. Zhao, G. Liang, Q. Yang, M. Li, Q. Huang, B. Dong, Confining aqueous Zn-Br halide redox chemistry by Ti_3C_2TX MXene, ACS Nano 15 (2021) 1718–1726.

[58] T. Kosmala, A. Baby, M. Lunardon, D. Perilli, H. Liu, C. Durante, C. Di Valentin, S. Agnoli, G. Granozzi, Operando visualization of the hydrogen evolution reaction with atomic-scale precision at different metal-graphene interfaces, *Nat. Catal.* 4 (10) (2021) 850–859.

[59] Y. Liu, L. Li, L. Wang, N. Li, X. Zhao, Y. Chen, T. Sakthivel, Z. Dai, Janus electronic state of supported iridium nanoclusters for sustainable alkaline water electrolysis, *Nat. Commun.* 15 (1) (2024) 2851.

[60] J. Li, J. Hu, M. Zhang, W. Gou, S. Zhang, Z. Chen, Y. Qu, Y. Ma, A fundamental viewpoint on the hydrogen spillover phenomenon of electrocatalytic hydrogen evolution, *Nat. Commun.* 12 (1) (2021) 3502.

[61] J. Dai, Y. Zhu, Y. Chen, X. Wen, M. Long, X. Wu, Z. Hu, D. Guan, X. Wang, C. Zhou, Hydrogen spillover in complex oxide multifunctional sites improves acidic hydrogen evolution electrocatalysis, *Nat. Commun.* 13 (1) (2022) 1189.

Crystal Facet-Induced Reconstruction of MoN-Supported Co Pre-Catalysts for Optimized Active Sites and Enhanced Alkaline Hydrogen Evolution

Chaoran Pi[a, f #], Difei Leng[b, #], Xuming Zhang[c, d, *], Shuangjie Wu[e], Yun Li[e], Li Huang[e], Zhihong Liu[a], Paul K. Chu[d, *] and Kaifu Huo[f, *]

[a] Chaoran Pi and Zhihong Liu
Key Laboratory of Optoelectronic Chemical Materials and Devices, Ministry of Education, School of Optoelectronic Materials & Technology, Jianghan University, Wuhan 430056, China
[b] Difei Leng
State Key Laboratory of Silicate Materials for Architectures, Wuhan University of Technology, Wuhan 430070, China
[c] Xuming Zhang
The State Key Laboratory of Refractories and Metallurgy, Institute of Advanced Materials and Nanotechnology, Wuhan University of Science and Technology, Wuhan 430081, China
[d] Xuming Zhang, and Paul K. Chu
Department of Physics, Department of Materials Science and Engineering, and Department of Biomedical Engineering, City University of Hong Kong, Tat Chee Avenue, Kowloon, Hong Kong, China
[e] Shuangjie Wu, Yun Li, and Li Huang
Guizhou Wujiang Hydropower Development Co., Ltd., Guizhou 550002, China
[f] Chaoran Pi and Kaifu Huo
Wuhan National Laboratory for Optoelectronics (WNLO), School of Optical and Electronic Information, Huazhong University of Science and Technology, Wuhan 430074, China; Research Institute of Huazhong University of Science and Technology in Shenzhen, Shenzhen 518057, China.

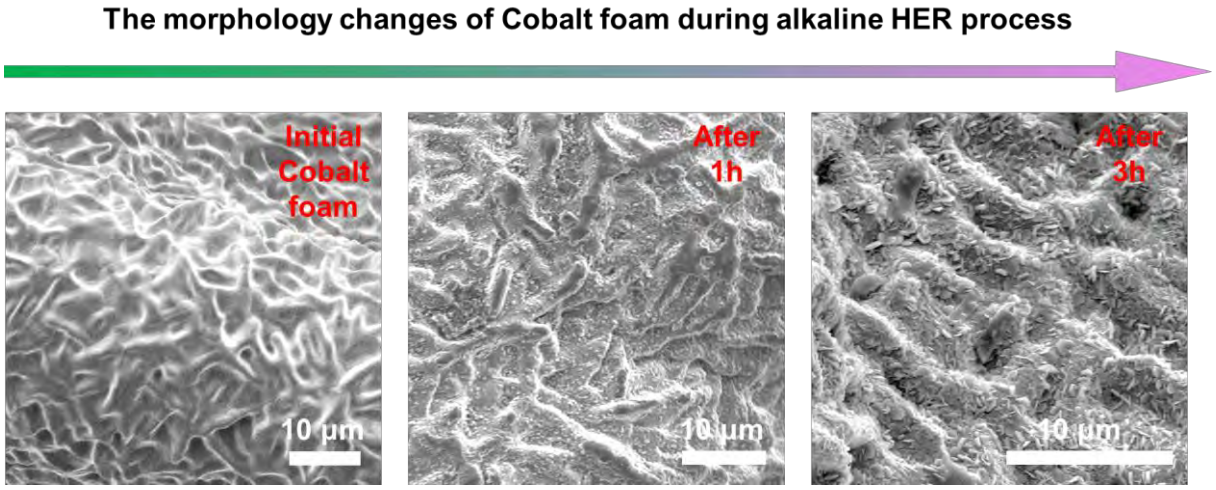

Figure S1. SEM images of Co foam at different stages by chronopotentiometry method under alkaline HER conditions, which indicate the transformation from Co to $Co(OH)_2$ under alkaline HER conditions is an inevitable and universal phenomenon.

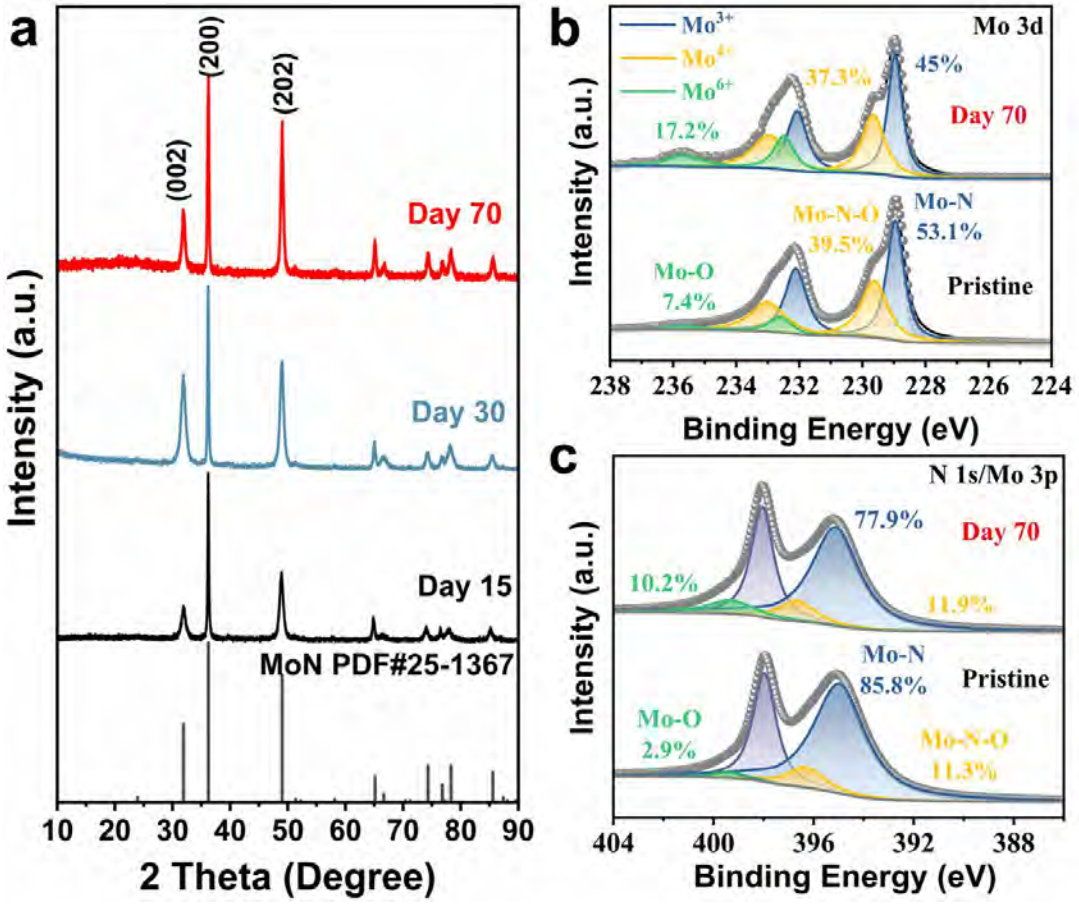

Figure S2. Characterization of pure MoN after soaking in 1M KOH solution for 15, 30 and 70 days. (a) Corresponding XRD results; (b) Mo 3*d* XPS spectra and (c) N 1*s* XPS spectra of pristine MoN and the sample soaked in 1M KOH for 70 days, respectively. The above results demonstrate that MoN exhibits excellent chemical stability in alkaline electrolyte.

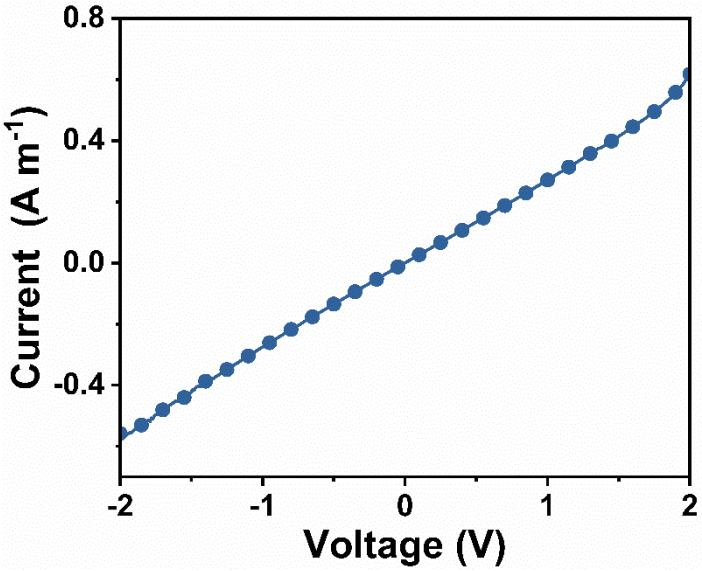

Figure S3. The I-V curve of pure MoN. The conductivity of MoN can be calculated by the equation: $\sigma=I/Vd$. Where I is the collected current (A), V is the voltage applied between the two test points (V), and d is the distance between the test points (m). The calculated σ_{MoN}=58.8 S m^{-1}, indicating the excellent conductivity of MoN.

Based on the conclusions in Figure S2 and Figure S3, MoN exhibits good chemical stability and excellent electron transport capability, making it an ideal substrate material for studying the directional reconstruction of pre-catalysts.

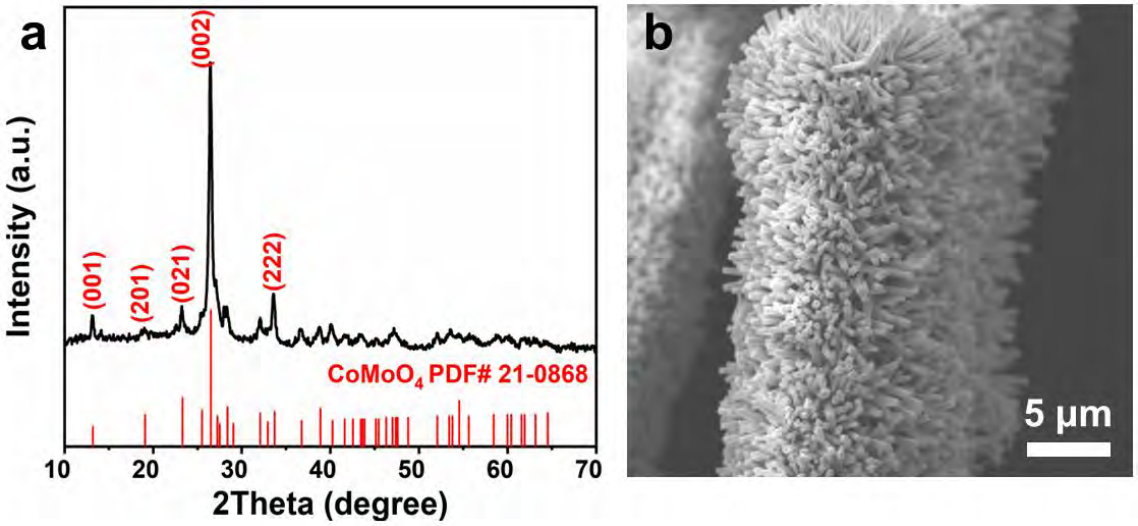

Figure S4. (a) XRD pattern and (b) SEM image of $CoMoO_4$ nanorod array precursor.

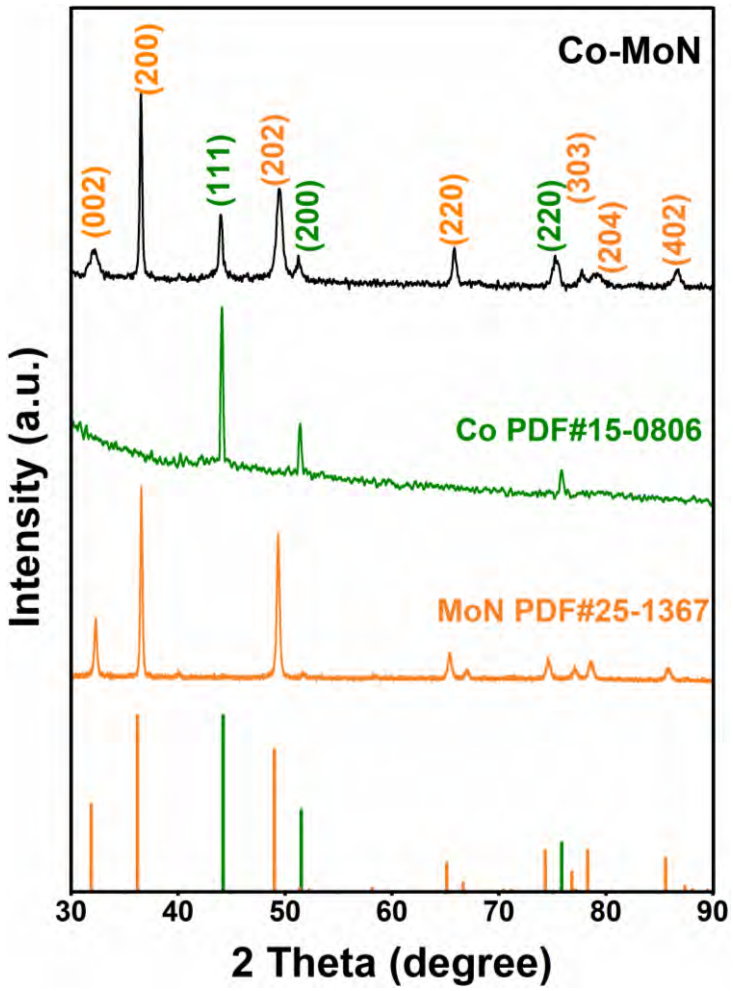

Figure S5. XRD pattern of the synthesized Co-MoN.

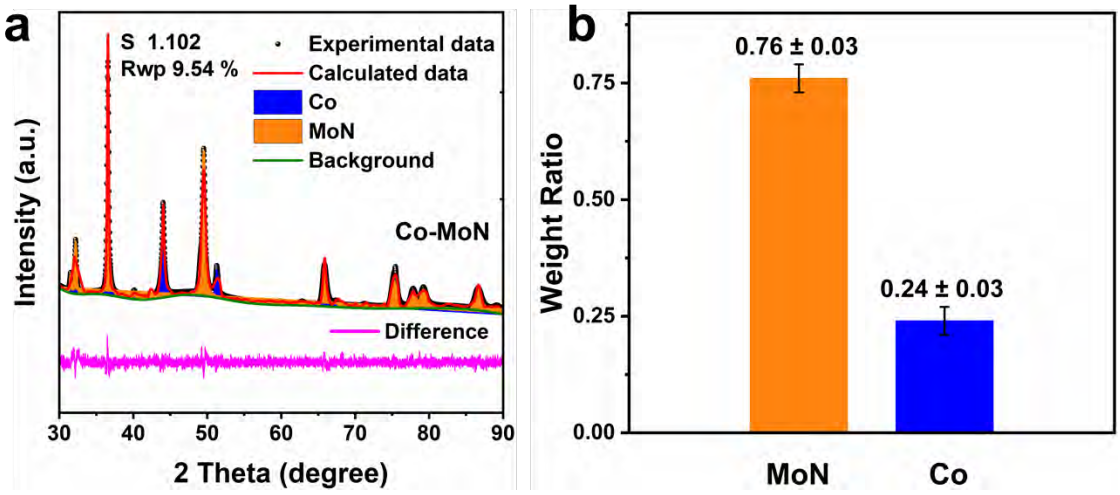

Figure S6. XRD refinement results of as-synthesized Co-MoN calculated by the Rietveld method. The molar ratio or Mo to Co is about 1:0.6. The error bars are generated from the standard error of the mean derived from three measurements.

Table S1 The elemental composition of Co-MoN determined by the ICP-MS test

Element	1st test	2nd test	3rd test	Average result
Co	2.9 mg/L	4.2 mg/L	3.1 mg/L	3.4 mg/L
Mo	9.4 mg/L	8.3 mg/L	10.1 mg/L	9.3 mg/L

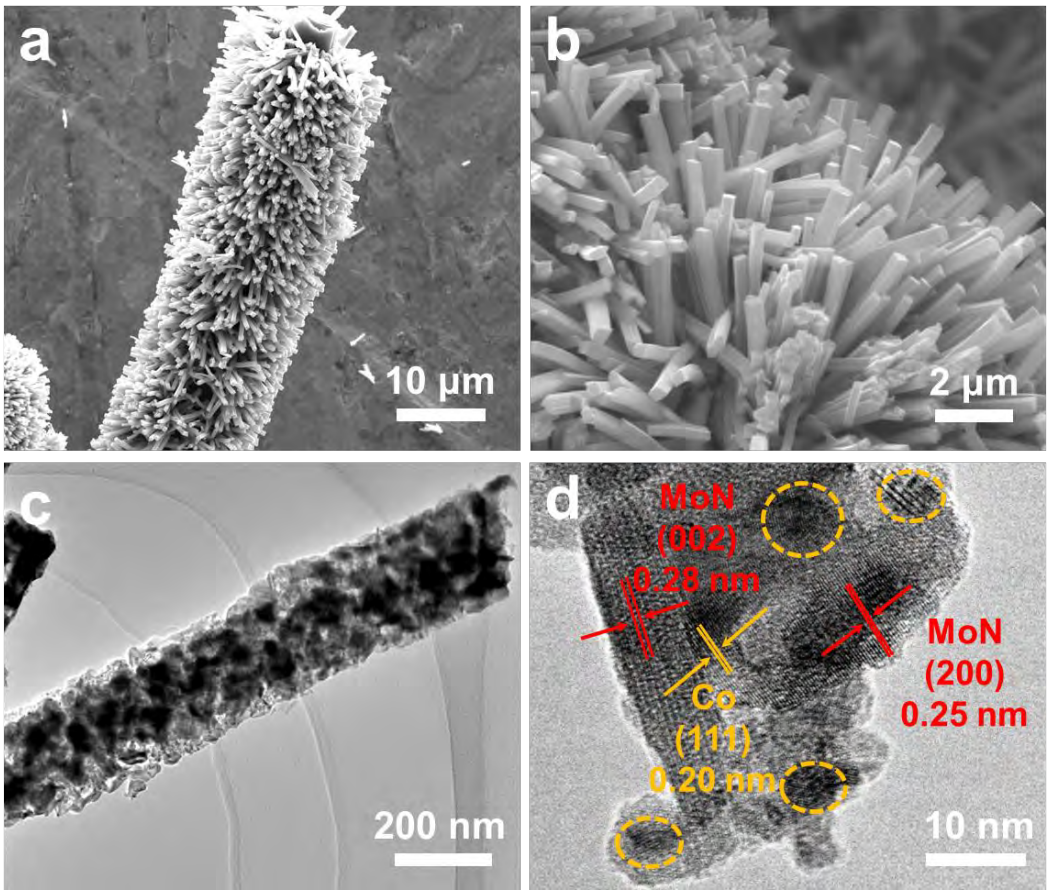

Figure S7. (a, b) SEM images and (c, d) TEM images of Co-MoN.

Figure S8. Pictures of the pristine CC, $CoMoO_4$ on CC, and Co-MoN on CC. The mass loading of Co-MoN on CC is 8.0 mg cm^{-2}.

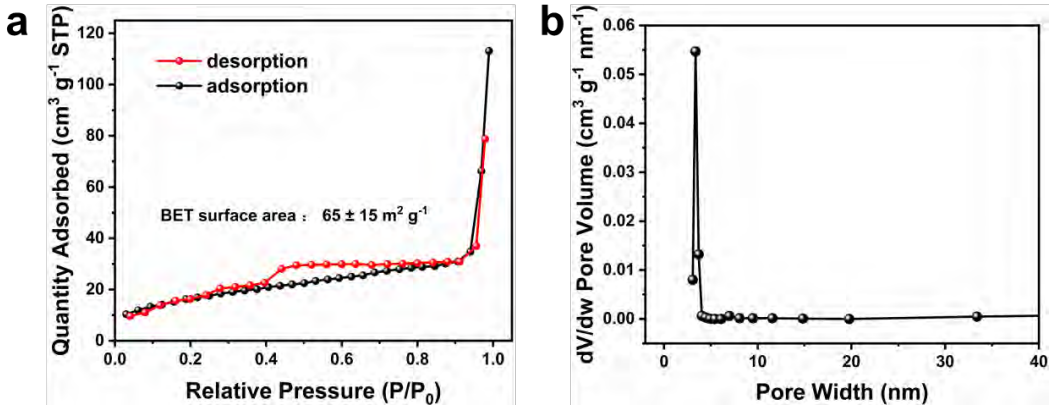

Figure S9. (a) N_2 adsorption/desorption isotherms and (b) the pore size distribution of the as-prepared Co-MoN nanorod arrays.

The BET surface area is calculated from the following two formulas: $\frac{1}{V(\frac{P}{P_0}-1)} = \frac{C-1}{V_m} \cdot \frac{P}{P_0} + \frac{1}{V_m}$.

V: Adsorbed volume of nitrogen gas (cm^3/g or mol/g) at relative pressure P/P₀; P/P₀: Relative pressure (P is the pressure of nitrogen during adsorption, and P₀ is the saturated vapor pressure); V_m: Volume of gas adsorbed to form a monolayer (cm^3/g or mol/g); C: BET constant, related to the heat of adsorption; P_0: Saturation vapor pressure of nitrogen gas at the temperature of the experiment.

Plot $\frac{1}{V(\frac{P}{P_0}-1)}$ on the y-axis and $\frac{P}{P_0}$ on the x-axis. The resulting plot should be a straight line, and the slope and intercept of the line can be used to calculate $\mathbf{V_m}$ (the monolayer adsorbed volume) and **C** (the BET constant). So according to the fitting result. $\mathbf{V_m}$**=15.116 ± 3.6.**

Then the BET surface area: S= $\frac{V_m N_A A}{22414}$

S = BET surface area (m^2/g); V_m = Monolayer adsorbed volume (cm^3/g or cm^3g); N_A = Avogadro's constant (6.022×10^{23} mol^{-1}); A = Area occupied by one nitrogen molecule (usually 0.162 nm^2 or 1.62×10^{-20} m^2 per nitrogen molecule); 22414 = A constant with units of cm^3/mol, used to convert gas volumes at STP to moles.

Finally, the calculated BET surface area is about **65 ± 15 m^2 g^{-1}**

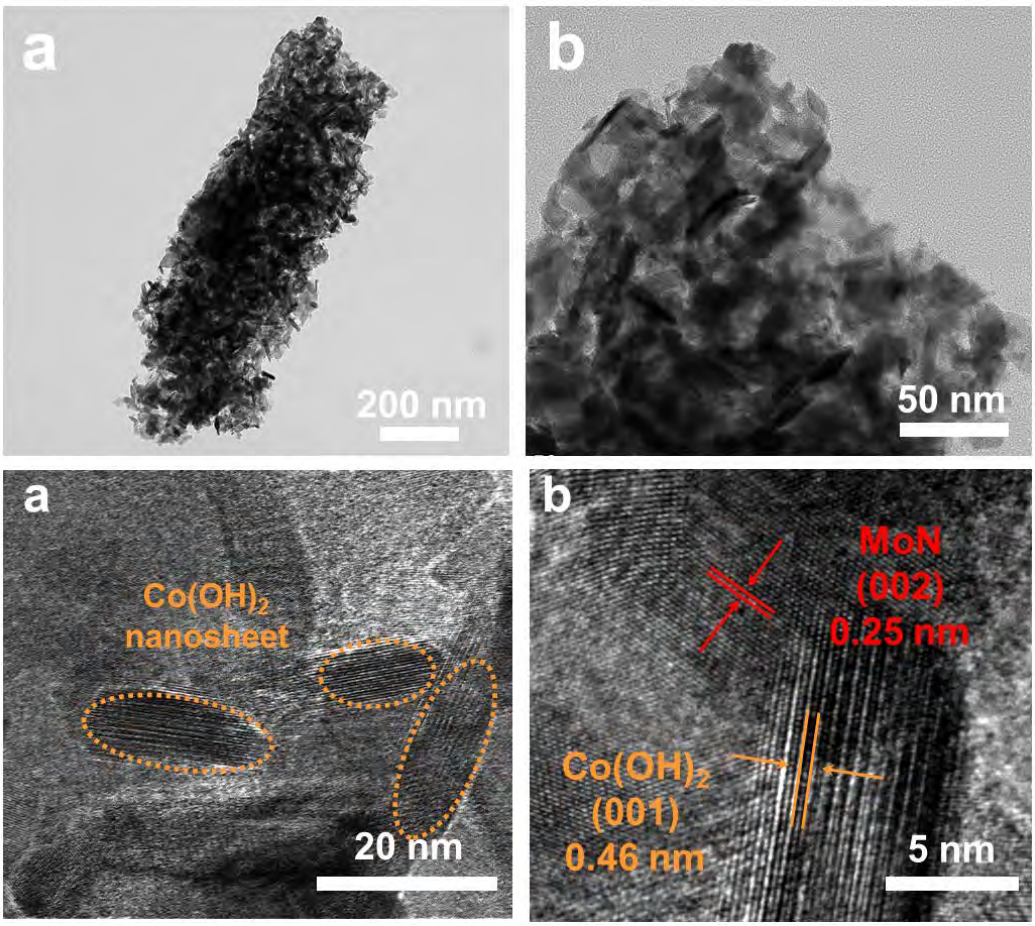

Figure S10. (a-b) TEM images and (c-d) HR-TEM image of Co-MoN after chronopotentiometry test. Different form the pristine quadrangular nanorods structure, the nanorods are covered by nanosheets.

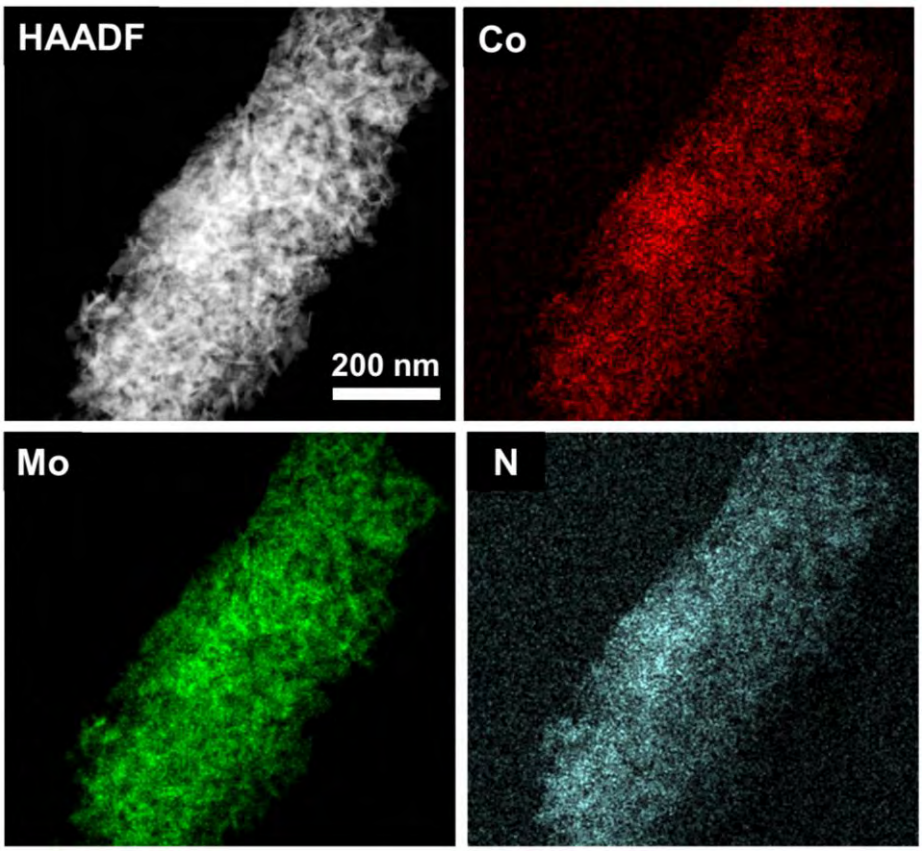

Figure S11. HAADF image and elemental maps of the Co-MoN nanorod after CP test.

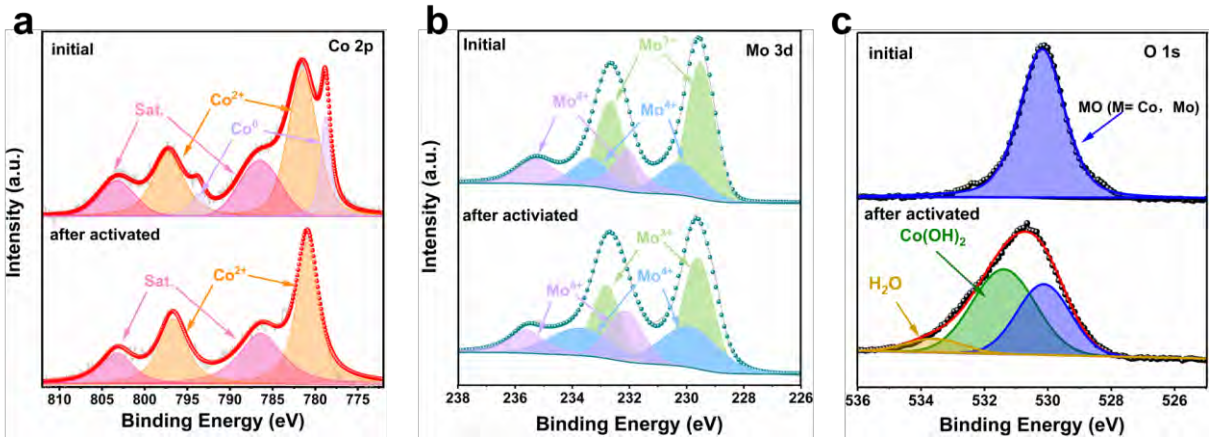

Figure S12. (a) Co 2*p* (b) Mo 3*d* and (c) O *1s* XPS spectra of Co-MoN before and after the electrochemical activation.

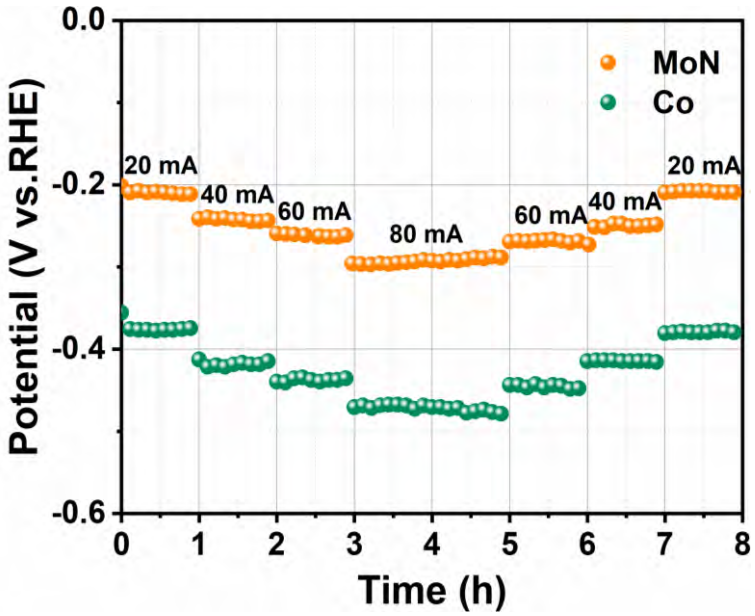

Figure S13. Multi-step constant current tests of the Co and MoN electrodes, confirming that the overpotentials required by both the Co metal and single-phase MoN electrodes to drive the same current do not change.

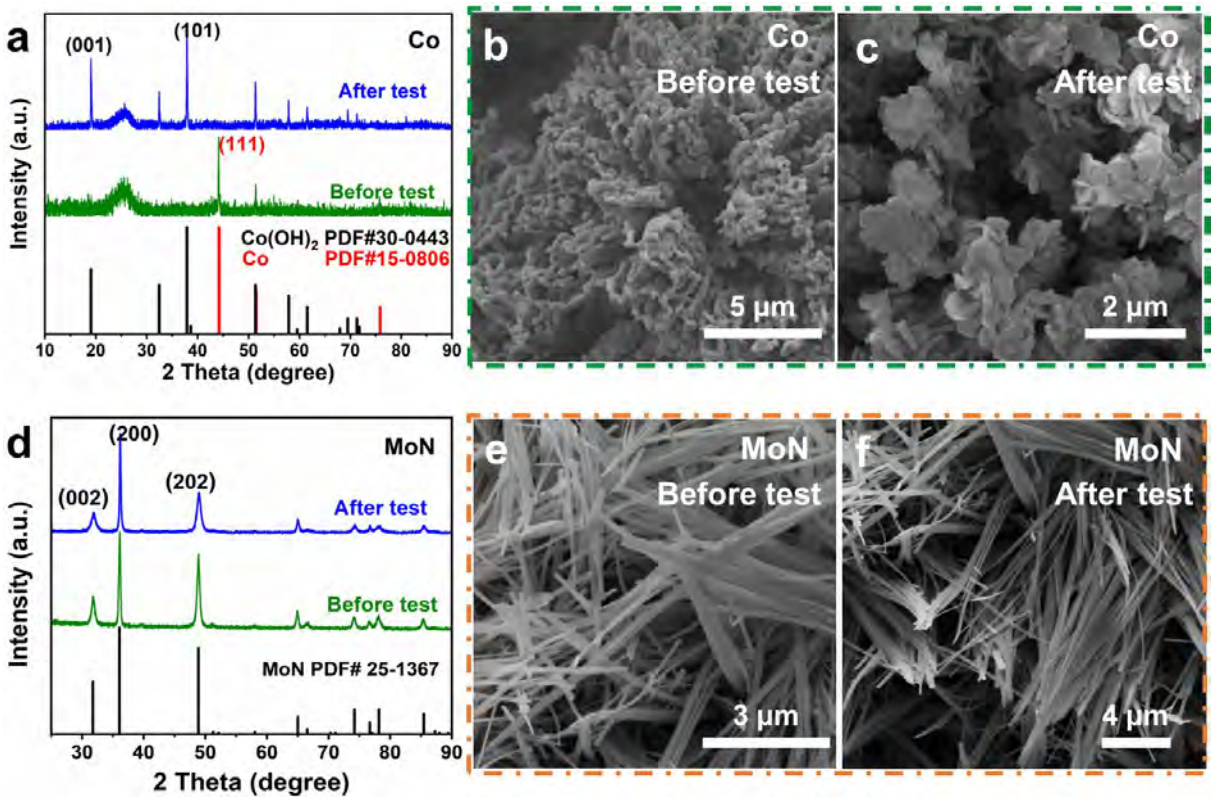

Figure S14. XRD spectra of (a) Co metal and (d) single-phase MoN electrode before and after chronopotentiometry test. Corresponding SEM images of (b, c) Co and (e, f) MoN. The results confirm that although there are no changes in the electrochemical performance, the Co electrode is converted completely into $Co(OH)_2$, while the composition and structure of MoN remain stable.

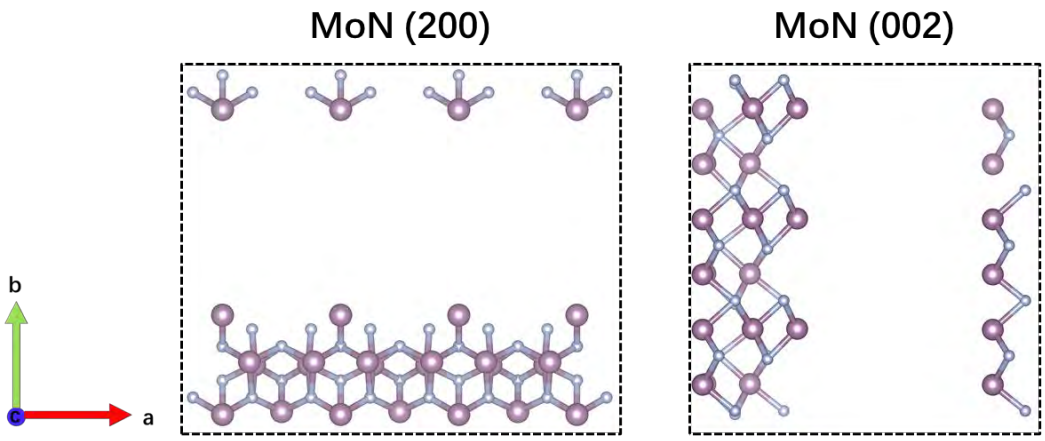

Figure S15. The MoN 1×1×3 supercell with a 5 Å vacuum layer in the xy plane exhibits periodicity solely along the z-direction but no periodicity in the xy plane. The energy of the (002) plane is calculated. The MoN 3×1×1 supercell with a 5 Å vacuum layer in the yz plane showing periodicity exclusively along the x-direction but no periodicity in the yz plane. The energy of the (200) plane is computed. DFT calculations confirm that the energy of the MoN (002) facet is 0.639 Ry lower than that of the MoN (200) facet.

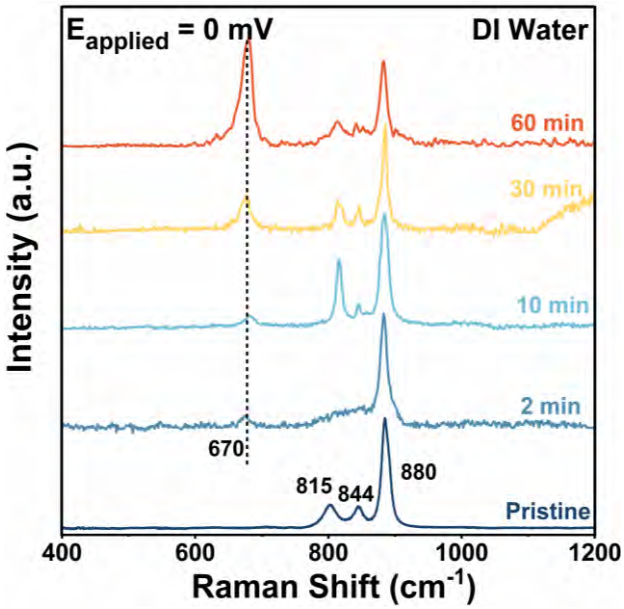

Figure S16. Time-dependent *in situ* Raman scattering spectra of the Co-MoN pre-catalyst in DI water with 0 V applied.

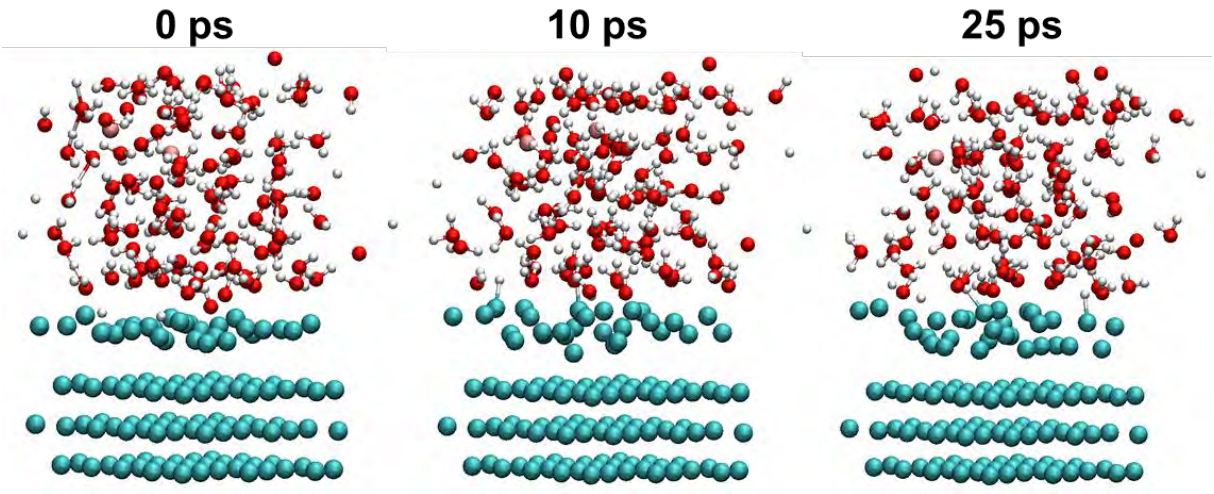

Figure S17. Snapshots taken in the classical molecular dynamics simulations of the cobalt metal-electrolyte (1 M KOH) system on the electrode surface: Without the applied bias at 0, 10 and 25 picoseconds.

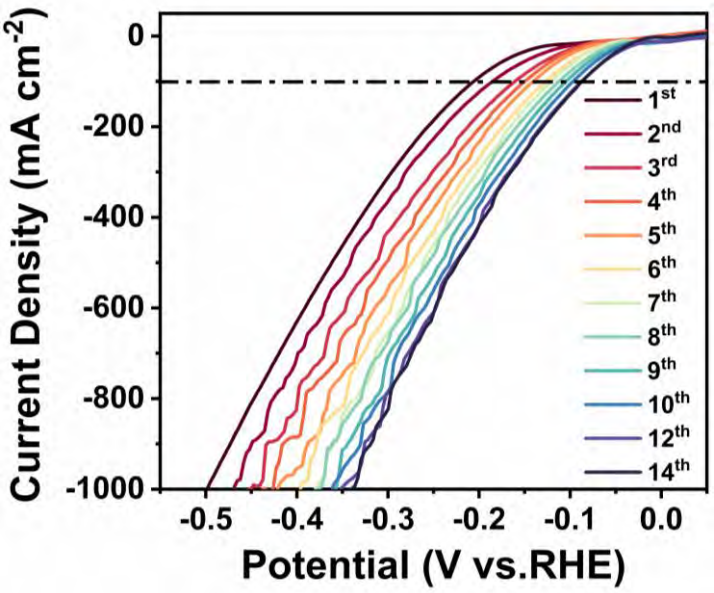

Figure S18. Consecutive LSV curves of the Co-MoN electrode for 14 cycles for potentials from -0.9 to -1.5 V *vs.* Hg/HgO at a scanning rate of 0.4 mV s^{-1} in 1 M KOH. Each scan takes 1500 s and the total testing time is about 6 hours.

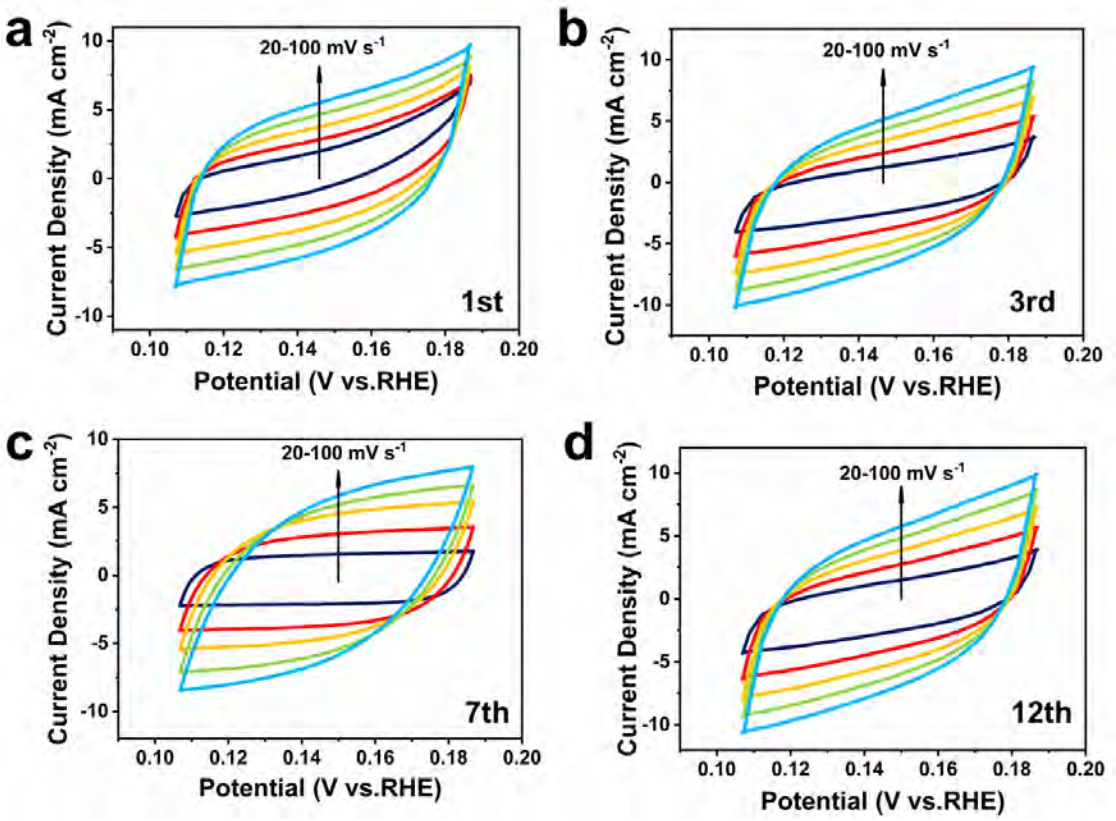

Figure S19. CVs acquired at different rates from 20 to 100 mV s^{-1} in the non-Faradaic potential region of 0.1-0.2 V *vs.* RHE from the Co-MoN electrode after 1st (initial), 3rd (after 1 hour), 7th (after 3 hours), and 12th (after 5 hours) successive LSV tests in 1 M KOH.

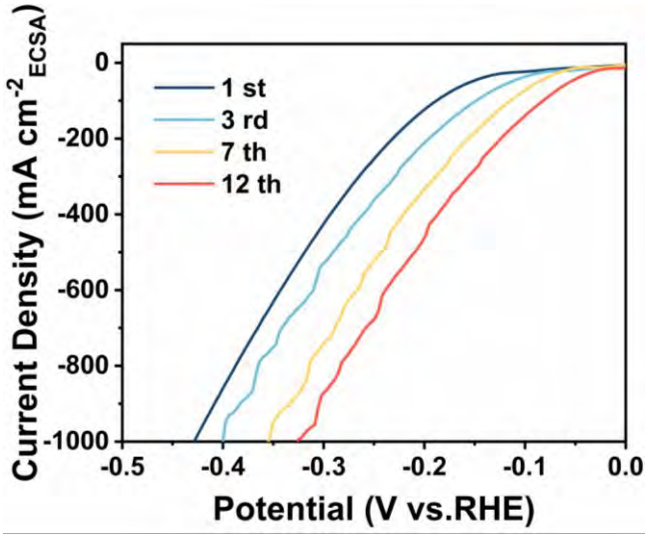

Figure S20. ECSA-normalized polarization curves of the Co-MoN pre-catalyst for the 1st 3rd 7th and 12th cycle.

Calculation of turnover frequency (TOF):

In this part, the TOF of the reconstructed $Co(OH)_2$-MoN and the commercial 20% Pt/C is calculated for comparison.

The turnover frequency can be calculated by the following formula:

$$TOF = \frac{\text{no. of total hydrogen turnovers/ cm}^2\text{ of geometric area}}{\text{no. of active sites/ cm}^2\text{ of geometric area}};$$

the molecules can be represented as:

$$(j\ \frac{mA}{cm^2})(\frac{1\ C\ s^{-1}}{1000\ mA})(\frac{1\ mol\ of\ e^-}{96485.3\ C})(\frac{1\ mol\ of\ H_2}{2\ mol\ of\ e^-})(\frac{6.022\times10^{23}\cdot H_2\ molecules}{1\ mol\ of\ H_2}) = (3.12\times10^{15}\ \frac{H_2\cdot s^{-1}}{cm^2}\ per\ \frac{mA}{cm^2})\times|j|;$$

the denominators can be represented as :(active sites per real surface area) × A_{ECSA}.

$$\text{Therefore, } TOF = \frac{(3.12\times10^{15}\ \frac{H_2\cdot s^{-1}}{cm^2}\ per\ \frac{mA}{cm^2})\times|j|}{(\text{active sites per real surface area})\times A_{ECSA}}$$

Then the active sites per real surface area can be calculated according to the mass loading and C_{dl} value:

For Pt/C:

active sites= 5×10^{-3} g (mass loading) × 20% (wt.% Pt) × $6.02\times10^{23}/195(M_{pt})=3.08\times10^{18}$ atoms cm^{-2}.

$$A_{ECSA} = \frac{162\times10^3\ \mu F\ cm^{-2}}{60\ \mu F\ cm^{-2}\ per\ cm^2_{ECSA}} = 2700\ cm^2_{ECSA}$$

For $Co(OH)_2$-MoN:

active sites= 0.8×10^{-3} × 76% (wt.% MoN) × $6.02\times10^{23}/110(M_{MoN})= 3.32\times10^{18}$ atoms cm^{-2}

$$A_{ECSA} = \frac{54\times10^3\ \mu F\ cm^{-2}}{60\ \mu F\ cm^{-2}\ per\ cm^2_{ECSA}} = 900\ cm^2_{ECSA}$$

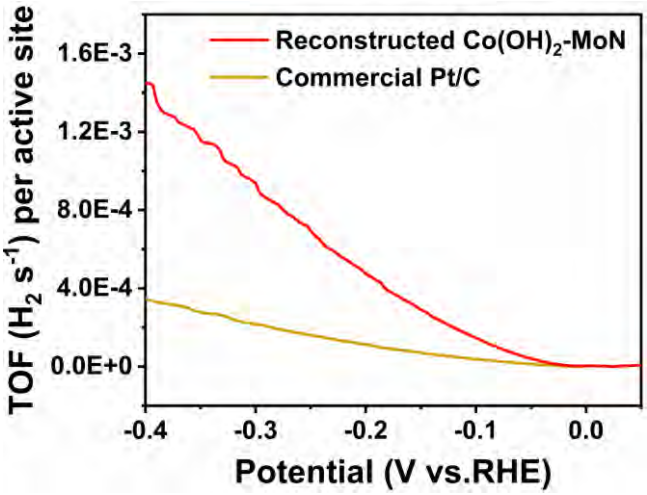

Figure S21. TOF values of the reconstructed $Co(OH)_2$-MoN and commercial Pt/C

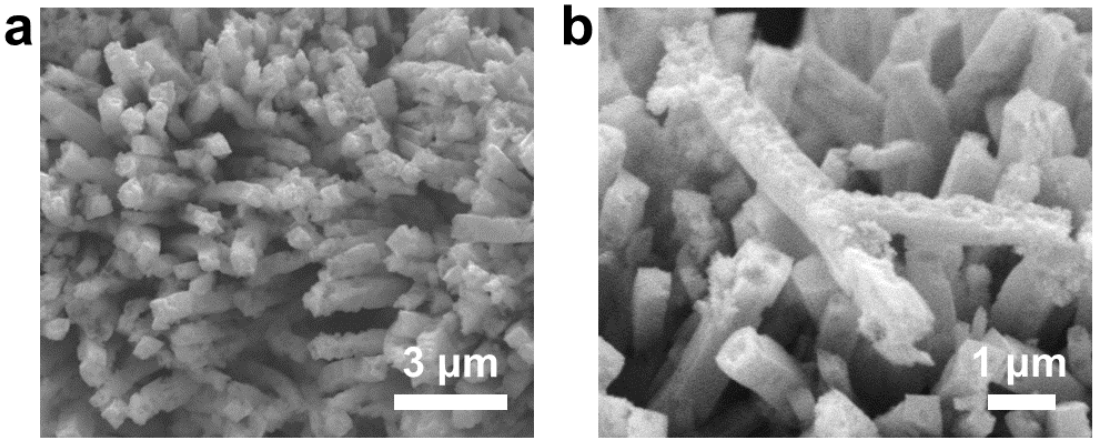

Figure S22. SEM images of the reconstructed $Co(OH)_2$-MoN electrode after immersion in 0.5 M HCl for 12 h.[1]

1, 2

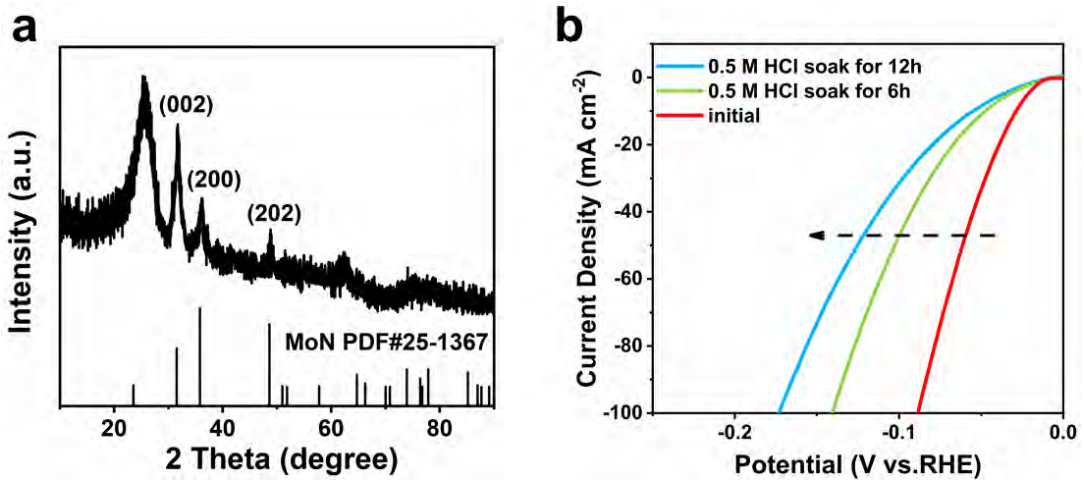

Figure S23. (a) XRD pattern of the reconstructed electrode after immersion in 0.5 M HCl for 12 h and (b) LSV tests of the electrode with pickling time confirming degradation of the catalytic activity.

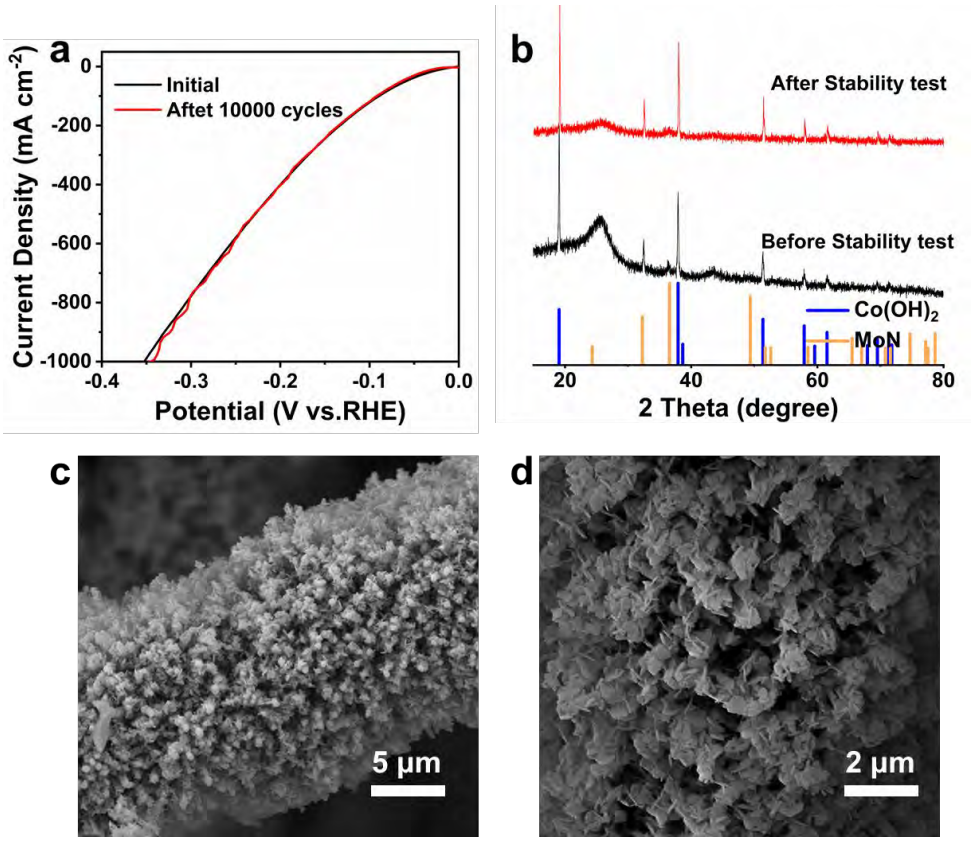

Figure S24. (a) Polarization curves (b) XRD patterns before and after 10000 CV cycles; (c-d) SEM images of the reconstructed $Co(OH)_2$-MoN catalyst after the stability test.

Faraday efficiency (FE):

The FE is calculated by the following formula: $FE = \frac{\frac{m}{22.4} \times n \times F}{I \times t} \times 100\%$, where the m, n, F, I and t stand for volume, charge transfer number for the formation of one H_2 molecular (n = 2), faradic constant (96485 C), applied current (0.1 A) and duration time.

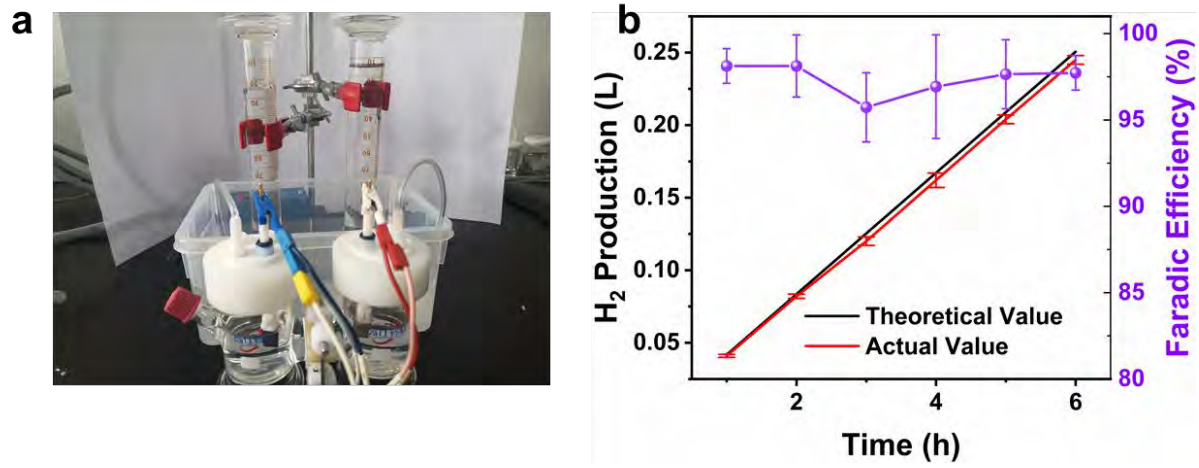

Figure S25. (a) Digital photograph of H_2 gas collection in three-electrode system; (b) The faradic efficiency of HER process calculated at 0.1A current for 6 h in three-electrode system. The error bars are generated from the standard error of the mean derived from three measurements.